2004-07-01

Time Blanking for GBT Data with RADAR RFI

Weizhen Dong
Brigham Young University - Provo

TIME BLANKING FOR GBT DATA WITH RADAR RFI

by

Weizhen Dong

A thesis submitted to the faculty of

Brigham Young University

in partial fulfillment of the requirements for the degree of

Master of Science

Department of Electrical and Computer Engineering

Brigham Young University

August 2004

BRIGHAM YOUNG UNIVERSITY

GRADUATE COMMITTEE APPROVAL

of a thesis submitted by

Weizhen Dong

This thesis has been read by each member of the following graduate committee and by majority vote has been found to be satisfactory.

Date	Brian D. Jeffs, Chair
Date	A. Lee Swindlehurst
Date	Karl F. Warnick

BRIGHAM YOUNG UNIVERSITY

As chair of the candidate's graduate committee, I have read the thesis of Weizhen Dong in its final form and have found that (1) its format, citations, and bibliographical style are consistent and acceptable and fulfill university and department style requirements; (2) its illustrative materials including figures, tables, and charts are in place; and (3) the final manuscript is satisfactory to the graduate committee and is ready for submission to the university library.

Date

Brian D. Jeffs
Chair, Graduate Committee

Accepted for the Department

Michael A. Jensen
Graduate Coordinator

Accepted for the College

Douglas M. Chabries
Dean, College of Engineering and Technology

ABSTRACT

TIME BLANKING FOR GBT DATA WITH RADAR RFI

Weizhen Dong

Department of Electrical and Computer Engineering

Master of Science

The 1215 MHz to 1400 MHz band is important for radio astronomers to observe redshifted extragalactic hydrogen ionic (HI). Observations at these frequencies are complicated by radio frequency interference (RFI) from strong man-made transmissions such as the ARSR-3 Air Surveillance Radar. In this thesis, we characterize some data files recorded at the National Radio Astronomy Observatory (NRAO) at Green Bank, West Virginia, USA, where this RADAR system causes significant data corruption. Using this data, we present a blanking technique to separate RFI from cosmic signal.

There are generally two blanking approaches, time window blanking and detected pulse blanking. Compared with time window blanking, the advantage of detected pulse blanking is that the loss of integration time is much less (i.e. less data is discarded). But some pulses fail to be blanked because they are too weak to detect. So in order to blank weak pulses, it is desirable to optimize detection performance. In this work, we will combine these two blanking techniques and present a new Bayesian

algorithm which combines Kalman tracking with pulse detection. This new algorithm will help to locate the weaker or missed detections, so as to help improve the performance of pulse blanking.

ACKNOWLEDGMENTS

Many people have contributed to the successful completion of this thesis. I would like to express appreciation to my thesis and academic advisor, Dr. Brian D. Jeffs, for his guidance and advice. I have also received much help from the other members of my graduate committee, Dr. A. Lee Swindlehurst and Dr. Karl F. Warnick. I also would like to express my sincere gratitude towards Dr. Rick Fisher in the Green Bank, for his generous help during the course of this work.

I also wish to thank my parents and my older sister, for their support and encouragement. Above all, I appreciate the loving support and devotion of my husband, Carlos. I dedicate this thesis to them.

Contents

List of Figures

Chapter 1

Introduction

Radio astronomical observation is more and more frequently polluted by all kinds of radio frequency interference (RFI) such as aeronautical RADAR and distance measuring equipment (DME) from aircraft at 960-1400 MHz, pager and cellular phone signals below 1000 MHz, television and FM radio transmitters, microwave ovens, and a variety of satellite transmitters including Iridium, GLONASS and GPS. Astronomers and engineers are facing unprecedented challenges as they attempt to solve the problem of RFI mitigation.

Different techniques must be devised to accommodate the wide range of interferences and science goals [1][2]. RFI mitigation can be placed in four categories: Time blanking, adaptive cancelling, interferometric nulling, and post-correlation analysis. Ground-based aviation RADAR (GBAR) transmissions occur in the important red shifted Hydrogen line observation frequency range from 960-1400 MHz. These signals may dramatically disturb radio astronomical observations by wrongly influencing spectrum estimation. However, the induced pollution is often transient, so for radio astronomy observation, one solution is to simply not include RADAR pulse corrupted data samples during spectrum estimation. This technique, termed "time-blanking" [3][4], remains efficient as long as RFI pulses are reliably detected and the corrupted samples are a small percentage of the whole data set.

The ARSR-3 Air Surveillance RADAR is an example of one such interfering system which affects observations at the Green Bank Telescope (GBT). The transmit pulse for this system is 2 microseconds long with a 1292 MHz carrier and an average repetition rate of 341 Hz. Pulses are easily seen at the GBT through the RADAR

antenna sidelobes, and are very strong when the RADAR beam is directly pointed to local terrain features, such as the mountain ridge about 8km west of the GBT or a reflecting object, such as an aircraft.

Since the RADAR system operates continuously, observing near 1292 MHz requires that data containing interfering pulses must be removed, or blanked. There are two popular techniques, time window blanking and detected pulse blanking. Time window blanking is implemented by not accumulating spectra that has any of the input data extending into the time interval. Pulse blanking operates only when a pulse is detected and only for a period which equals the length of the pulse.

This thesis will focus on developing an algorithm to help improve performance of pulse detection for use by a pulse blanking process. The improved algorithm will exploit knowledge of the prior probability distribution of the pulses derived from a Kalman tracker, so as to improve the performance of pulse blanking.

1.1 Problem Statement

To illustrate the interference problem addressed in this thesis, we present some 1292 MHz data recorded at the GBT which clearly shows the RADAR signal. This data was recorded on the GBT by Dr. J. Richard Fisher, who also provided some valuable analysis of the data in [5][6]. Figure 1.1 shows pulse intensity as a function of delay relative to the first arriving pulse. Strong pulses can be seen out to a delay of 135 microseconds, most of which are due to reflections from the hilly terrain around the GBT. The group of returns at 430 microseconds is probably from an aircraft.

Nothing can be done with the data prior to 135 microseconds, so it is all simply excised or blanked. Here we employ time window blanking by not accumulating spectra that has any of the input data extending into the time interval to be blanked. Figure 1.2 shows the blanking window beginning 20 microseconds before and ending 150 microseconds after the first pulses arriving from the radar. This simple window blanks the strong pulses from terrain reflection.

However, the weak pulses at 345 and 430 microseconds are very isolated aircraft echoes, and the goal is to remove only the few corrupted data samples containing the

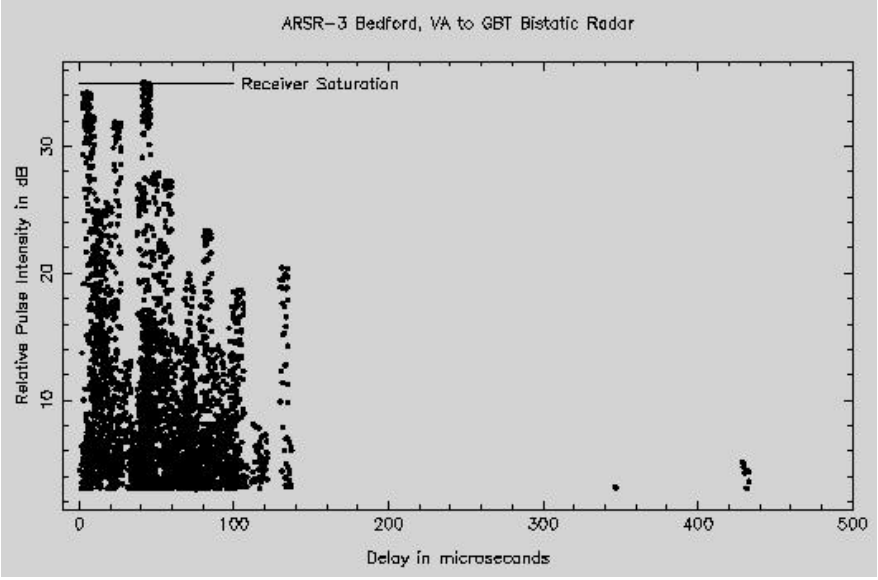

Figure 1.1: Pulse intensity as a function of delay from the directly arriving pulse.

pulses, while preserving neighboring time bins. Also, some weaker echoes may not be easily detected, but would still bias spectral estimates if not removed. So for long-delay pulse reflections from aircraft which fall outside of the selected blanking time window, we will apply detected pulse blanking. Pulse blanking removes data only when a pulse is detected and only for a period which equals to the length of the pulse.

The goal of this work is to develop an advanced "intelligent" algorithm approach to detecting these echoes, so more corrupted aircraft data can be removed without sacrificing neighboring data unnecessarily. The proposed algorithm will utilize time-history information across multiple RADAR antenna sweeps to built track estimate for aircraft motion. These track data will be used to improve echo detection performance.

The GBT experiments present in Chapter 6 demonstrate that detected pulse blanking is a useful technique for rejecting transient pulse reflections that fall outside of the selected time window, in combination with time window blanking for long-term corrupted data.

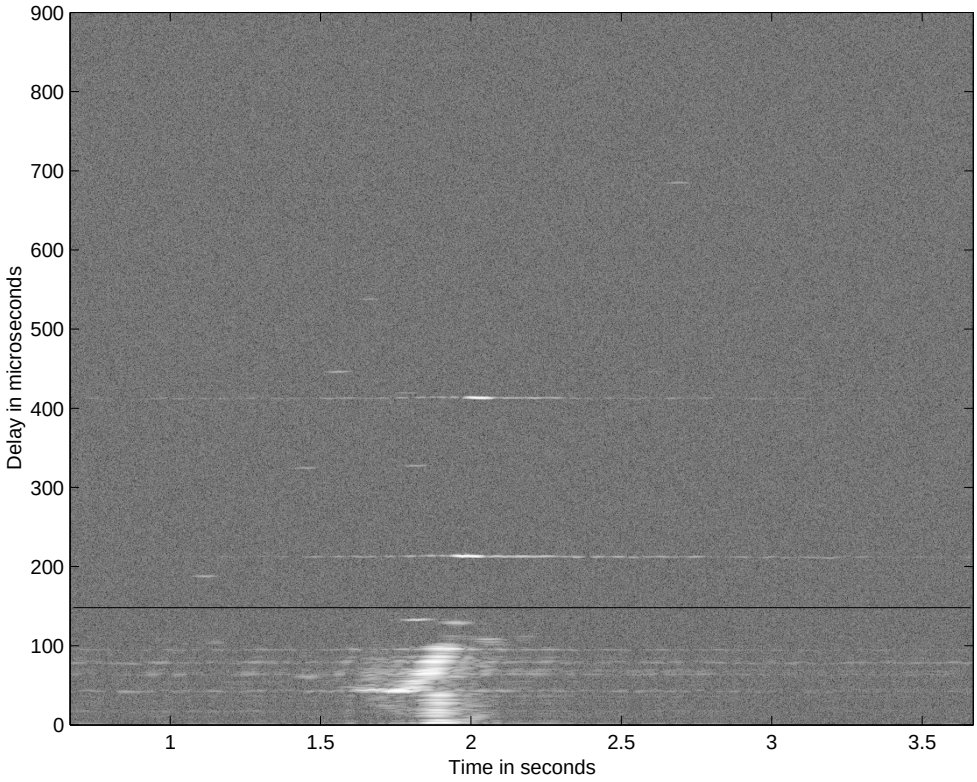

Figure 1.2: Time blanking window.

1.2 Related Work

There have been several previous studies on interference mitigation technique in radio astronomy. Leshem and Veen formulate the astronomical problem in an array signal processing language and provide an introduction to some elementary algorithms from that field [7][8]. Ellingson and Hampson have tested pulse-detection and blanking of radar at Arecibo and achieve 16 dB of suppression but find that undetected pulses limit performance [9][10]. Research by Fisher [5] at the GBT has demonstrated that about 10% and 0.4% of the spectra were rejected in the integration by using time window blanking and detected pulse blanking, respectively. This research suggests that detected pulse blanking does play a role in radar rejection in combination with time window blanking for rejecting transient pulse reflections that fall outside of the selected time window.

1.3 Approach

The Kalman Filter is an established technique widely applied in the fields of navigation, guidance, satellite orbit determination, aircraft and missiles tracking, etc. The main goal of this work is to present a new technique, which uses Kalman tracking to predict the position of moving aircraft. This prediction can be used to form not only predict regions for the next expected echoes, but also a prior probability distribution for the presence of the next echoes, which is then applied to improve echo detection performance, and further to improve blanking performance.

The Kalman tracker can be used for both real-time process and post processing. Real-time processing blanks the corrupted data before detection, using only prediction regions derived from the Kalman tracker. It only takes advantage of time-history information without the need to process the current data prior to blanking. By contrast, post processing blanks after detection. In this case, the blanked area should be smaller and more accurate than the one for real-time because both prediction information for the previous data and detection information for the current data are used.

1.4 Thesis Organization

This work first presents a description to characterize the 1292 MHz RADAR signal seen at the GBT. After that, we discuss the development of the proposed pulse detection technique, which includes matched filtering and time alignment by Constant False Alarm Rate (CFAR) detection of the first arriving pulses. The CLEAN algorithm is introduced as a technique used to locate single echo source points when many range-azimuth bins exceed the threshold due to the RADAR beam pattern sidelobes. The principle of Kalman filtering is discussed as a method of tracking the moving aircraft. Finally we propose the idea of combining Kalman tracking with pulse detection for better echo detection and blanking performance, and give experimental results for both simulation data and real RADAR data sets from the GBT.

1.5 Summary of Contributions

The original contributions of this thesis are as follows:

- Chapter 3

    1. Presents a matched filter followed by Constant False Alarm Rate (CFAR) detection of the first arriving pulse to align data in range-bearing form.
    2. Proposes an adaptation of the CLEAN algorithm to locate single echo source points when many range-azimuth bins exceed the threshold due to the RADAR beam pattern.

- Chapter 4

    1. Sets up an extended Kalman filter model for aircraft tracking.
    2. Proposes a tracking management system for dynamical multi-objective tracking.

- Chapter 5

    1. Proposes a Bayesian prior probability distribution model for echo pulses using knowledge from the Kalman tracker.
    2. Proposes a new idea of a variable threshold for the CLEAN algorithm detection step according to the prior probability of the pulses.
    3. Proposes a new algorithm which compares tracking with pulse detection to improve the performance of pulse detection.

- Chapter 6

    1. Uses Monte-Carlo simulation to compare the performance improvement of the new algorithm over the conventional one, and gives an analysis of the tradeoff between P_{FA} and P_D for the new Bayesian detection scheme.
    2. Demonstrations of the new algorithm using real data are presented to illustrate performance.

3. Compares the performance of detected pulse blanking using the new Bayesian detection scheme with the traditional time window blanking.

Chapter 2

Characterization of the 1292 MHz RADAR at the GBT

In this work, we focus on the 1292 MHz RADAR signal seen at the GBT. This signal is used for valuable commercial or government purposes such as radio navigation, but to the radio telescopes at Green Bank it is seen as radio frequency interference (RFI), sometimes covering up weak radiation from celestial radio sources. The main intent of studying this RADAR signal is to aid engineering research into ways of separating such man-made RFI from cosmic signals. In this chapter, we discuss some of the radar characteristics and parameters which are important to the design of the proposed blanking technique.

2.1 Data Collection

The RADAR antenna is located 104 km south-southeast of Green Bank at an azimuth of 163.87 degrees relative to the GBT. The antenna sweep period is 12 seconds per rotation, and the beamwidth is approximately 1 degree. The data used for this work are A/D samples received by the RFI monitor station in the GBT, recorded by Dr. Rick Fisher and his colleagues [5]. There are two data sets which were recorded in 2002 and 2003, respectively.

The 2002 data set is unsigned 8-bit A/D samples with a sampling frequency of 10.81818 Msamp/s and includes 37 data files.

- Data files t2.dat through t17.dat were recorded primarily to get samples of the strongest radar pulse at number of different RF gain settings. Data were recorded in the afternoon of March 25, 2002, with a horn antenna pointed toward 177 or 320 degrees indicated azimuth.

- Data file t18.dat through t33.dat were recorded in the morning of March 26, 2002. The purpose of these measurements was to record full-sensitivity radar pulses reflected from surrounding terrain and nearby aircraft. The first nine files used receiving horn azimuths spaced by 60 degrees over the full azimuth range. Because the available computer memory limited each data sequence to about 5 seconds, a full 12-second run was not possible to record in a single file. So the last seven files contain data recorded at approximately three minute intervals with the horn pointed at 357 degree azimuth to look for moving targets in this direction.

- Data set t34.dat through t38.dat were recorded at approximately one minute intervals with the receiving horn pointed to indicated azimuth 357 degree in the morning of April 5, 2002. The purpose of these data were to look for aircraft passing north of the observatory by looking for echoes that move uniformly in delay and radar antenna azimuth position.

The 2003 data set contains continuous 10-minutes-data blocks sampled with a new data acquisition system running in Green Bank. It was recorded using essentially the same receiver and antenna conditions as 2002 data set. The main differences are that the new data rate is 10 Msamp/s, and the data are now signed 8-bit.

As we discussed in Section 1.1, we are only interested in the aircraft echo for detected pulse blanking, so we will mainly focus on data set t34.dat through t38.dat and the 2003 data set in this work.

2.2 Pulse Signature

The RADAR pulse is 2 microsecond long with a 1292 MHz carrier. This carrier was heterodyned to a frequency of approximately 6 MHz where it was sampled at 20 megasamples/sec using the internal clock of the PDA500 data acquisition board. A typical pulse signature sampled by the 8-bit A/D converter is shown in Figure 2.1. It can be seen that the transmitted pulse was distorted by multipath propagation along

the 104 km separation distance. In the later Section 3.1, we will use a function that closely matches this pulse signature to achieve better pulse sensitivity.

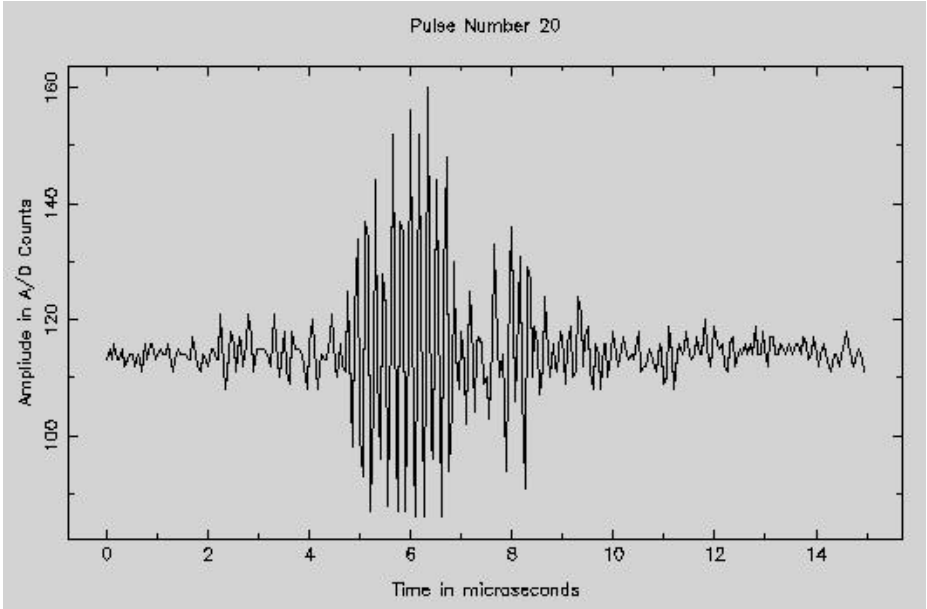

Figure 2.1: Pulse signature sampled by the A/D.

2.3 Pulse Repetition Rate

The measured average pulse repetition rate is 341.4 Hz with pulse time offset of an integer number of 100 microseconds in the repeating sequence of [0,4,0,3,1,2,1,3]. This offset is used to resolve ambiguities due to reflections beyond the range interval of 440 km set by the pulse spacing.

2.4 Pulse Arrival Times

By searching for the identifiable first arriving pulses, we reorganize the given data into a two-dimensional delay and radar antenna azimuth plot. Figure 2.2 shows a plot for a 2-second-data set with the measured pulse arrival times.

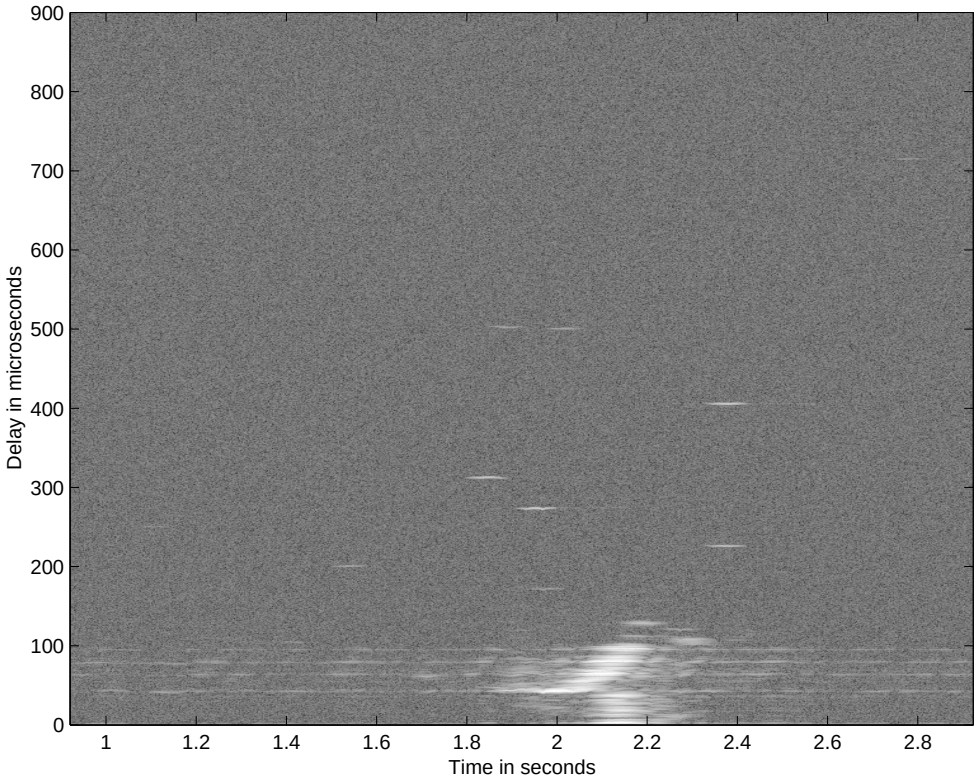

Figure 2.2: Pulse arrival times for about 2 seconds data set.

There are three notable features for this figure. First, pulses at constant arrival times are present during the full length of the data set. This is due to the fact that pulses can be seen through the transmit antenna sidelobes from the radar even when the radar beam is pointed well away from the Green Bank.

The second feature of Figure 2.2 is that the earliest pulses are not the most prevalent. The shortest path distance from the radar to GBT must produce the earliest arriving pulses. Since the GBT is about 400 meters below the elevation of the nearest diffraction obstacle about 12 km away, strong echoes from the high mountain ridge about 8 km west of the GBT are apparently longer paths with stronger signals.

The third notable feature of Figure 2.2 is the cluster of pulses around 2.2 seconds into the data sample. This is when the radar beam passes directly over Green Bank, and we clearly see reflection from local terrain features in addition to

the directly-arriving pulse, likely due to the sidelobe structure of the transmitting antenna beampattern. We acknowledge the help of Dr. Rick Fisher of NRAO in obtaining and interpreting this data.

Chapter 3

Pulse Detection

In this chapter, we will discuss the scheme for detecting an individual aircraft echo pulse. In the absence of multi-path and assuming additive spectrally-white Gaussian noise, the optimum detector of a single pulse is a filter matched to the transmitted pulse waveform, followed by pulse time alignment which reorganizes the one-dimensional data into two-dimensional range-bearing form. Then a modification of the well known CLEAN algorithm [11] will be used to accurately locate the single echo source points in the presence of broad transmit antenna sidelobe patterns.

3.1 Matched Filter

A matched filter [5][9] is a demodulation technique which achieves the maximum signal-to-noise ratio and the minimum probability of undetected pulse errors. Figure 2.1 shows that many of the pulses in the data set are severely distorted by multipath propagation before they are received, so the exact transmitted pulse which was designed for the RADAR system is unknown. We therefore introduce a model which is a reasonable approximation to the transmitted pulse. Figure 3.1 shows the approximation based on a rough manual fit of a Hamming window curve to the observed pulse in the time domain.

The matched filter is realized by convolving the data with this Hamming window function to achieve better pulse sensitivity. It is not strictly necessary to perform the matched filter in the time domain. An alternative [5] is to operate on the Fourier transformed input data, in which case the matched filter can be implemented as a multiplication of the frequency domain filter function, as opposed to a convolution of

the time series. This approach is theoretically equivalent to a time-domain matched filter.

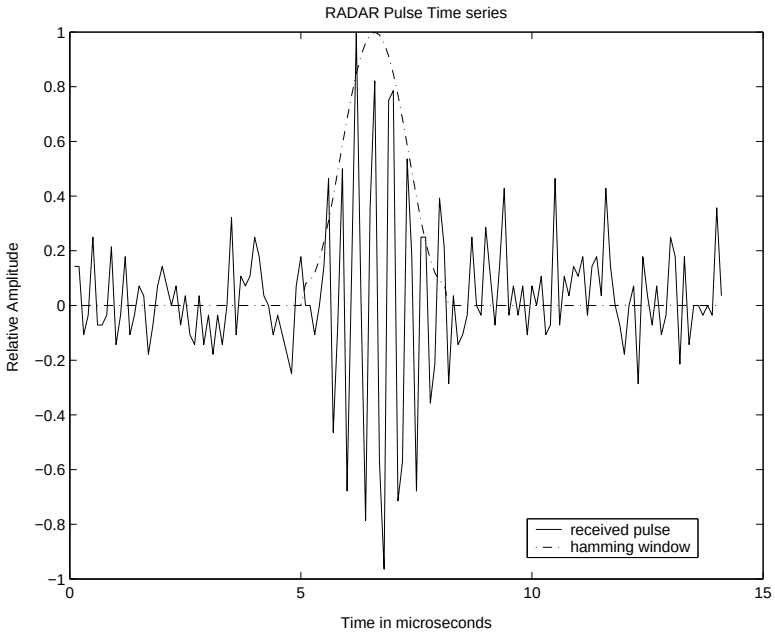

Figure 3.1: Hamming window function fit to a received pulse for the purpose deriving a pulse convolution.

Figure 3.2 shows the full digital receiver architecture. It is a maximum likelihood detector for a transmitted pulse with unknown phase in additive spectrally-white Gaussian noise (AWGN) [12] and the receiver includes three main steps:

1. The real valued RADAR signal $x(n)$ is converted to the real part $\mathrm{Re}\{x(n)\}$ and imaginary part $\mathrm{Im}\{x(n)\}$ by IQ demodulation [13][14].

2. A matched filter $h(n)$ is applied to the real and imaginary part separately.

3. The square of the complex magnitude, $y(n)$, forms the output of the matched filter.

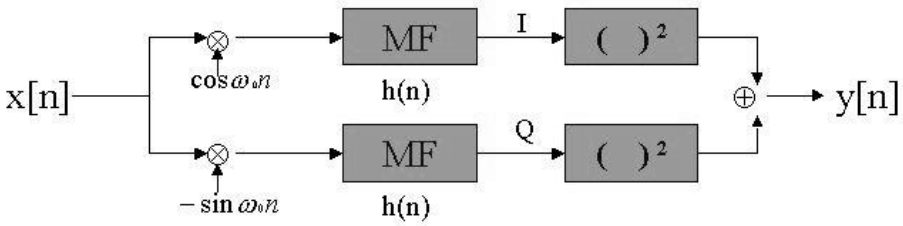

Figure 3.2: The full digital receiver architecture, which includes IQ demodulation part and matched filter part.

3.2 Pulse Time Alignment

To proceed further, we will reorganize the filtered time series data into two-dimensional delay-azimuth form by looking for the first arriving pulses as the time reference. It is more difficult to build a complete RADAR receiver to find the first arriving pulse in this case than for the true RADAR system. This is due to the following facts:

- The RADAR parameters are derived by analyzing the data, so we do not know exactly when the first arriving pulse comes.
- The long separation distance between the RADAR antenna and Green Bank makes the first arriving pulse distorted and weak, so it is sometimes not very obvious. Since the first arrival pulse may not be over a line-of-sight path, it can even be weaker than aircraft target echoes.
- In some data sets there were dropped or missing samples which corrupted time alignment even when it could once be established.
- All signal references, local oscillators, and sample clocks are asynchronous with respect to the RADAR transmitter.

This pulse time alignment problem is very critical because its accuracy will have strong effect on the performance of the CLEAN algorithm and Kalman tracking.

3.2.1 Initial Alignment

For simplicity, we will first make the alignment by approximating the first arriving pulse time based on estimated global parameters as follows:

- The measured average pulse repetition rate (PRF) is 341.4 Hz.
- The timing of the directly arriving pulses follows a time offset of an integer number of 100 microseconds in a repeating sequence of [0,4,0,3,1,2,1,3].

Then we can easily compute every pulse repetition interval (PRI) and reorganize the 1-D filtered RADAR data to a two-dimensional delay-angle (range-angle) form by using the derived first arriving pulses as the time references. Figure 3.3 shows the result of initial time alignment. Here the plot only includes about 3 seconds of data (about 90 degrees) while the radar beam passes directly over the GBT, because the echoes from the local terrain features and the aircrafts are most prevalent in this time period.

3.2.2 Improved Alignment using Constant False Alarm Rate Detection

Unfortunately, the initial alignment shown in our experiments was not accurate enough. Figure 3.3 shows that the first part of the data run was found to have a constant pulse arrival time. The drift in arrival times (notice the slope of the white lines) in the later part of the data was due to either a drift in the radar timing generator or the internal clock of the data acquisition board. Because of this, a more accurate pulse alignment had to be estimated directly from the filtered GBT data for each pulse interval. Here we will use a constant false alarm rate (CFAR) detection process to locate the first direct-path pulse arrival at the GBT for each pulse transmission. This first arrival pulse serves as a reliable time reference for the set of the echoes in the pulse interval.

A similar pulse detection algorithm was discussed in [9] to detect the onset of the pulse. Combined with the predicted position for first arriving pulses derived in Section 3.2.1, we will propose a CFAR algorithm for detecting first direct-path pulses as follows:

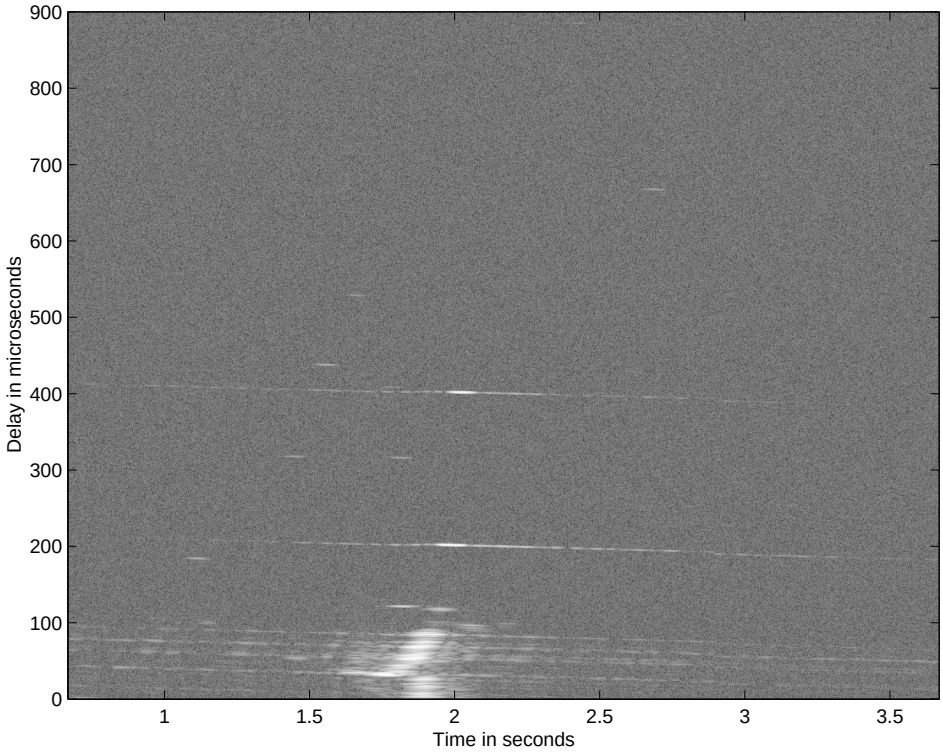

Figure 3.3: The result of initial time alignment. Note the echo pulse beampattern sidelobes (white stripes) are not perfectly horizontal. This indicates a drift error in transmit pulse timing detection.

1. Compute the "local" standard deviation σ of a sample sequence s_1 in the absence of radar pulses.

2. Detection of the first arriving pulse is declared when $s_2(t) \geq C\sigma$ occurs for the first time, where s_2 is a sample sequence inside a small window where a pulse probably occurs and C is the user-selected threshold which is set by maintaining an acceptable false alarm rate (FAR) for the χ^2 distributed noise in $y(n)$.

3. If there is no data in s_2 which satisfies $s_2(t) \geq C\sigma$, then we will choose the predicted time derived in Section 3.2.1 as the first arriving pulse.

In step 1, as Figure 3.4 shows, for every pulse interval we define a data sample sequence s_2 inside window 2 around the predicted pulse position. The size of window

2 is 2-3 times the pulse length and we only look for fine position detection of the first arrival within window 2. Then we define another 100-microsecond-long window 1 immediately prior to window 2 and calculate σ from the sample sequence, s_1, inside it. This guarantees that pulse signatures are effectively eliminated from s_1, so they do not bias the estimate of σ.

Although the true detection is probably not in the predicted position, at least it will be somewhere around the predicted one. So in steps two and three, we will look for the first sample of s_2 whose amplitude satisfies $s_2(t) \geq C\sigma$ and classify it as the beginning of a pulse. If there is no sample in s_2 which satisfies this condition, we will just decide that the predicted detection is a reliable one.

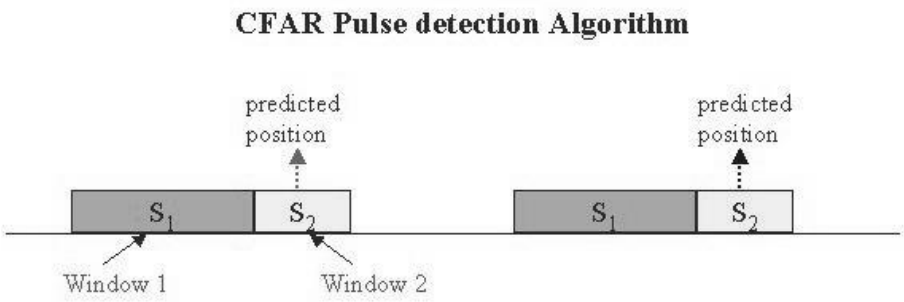

Figure 3.4: Improved pulse time alignment using a CFAR algorithm.

Figure 3.5 shows the resulting delay-azimuth image of improved time alignment using CFAR as first arrival pulse detection, with the same data set as figure 3.3.

3.3 Modified CLEAN Algorithm

To proceed further, we must locate the isolated echo source points because many range-azimuth bins exceed the threshold due to the RADAR antenna beam-pattern. The basic CLEAN method [15][16] is a very well-known algorithm used in the astronomical community to remove the severely sidelobe-contaminated point-spread beampattern from images produced by sparse array imaging systems.

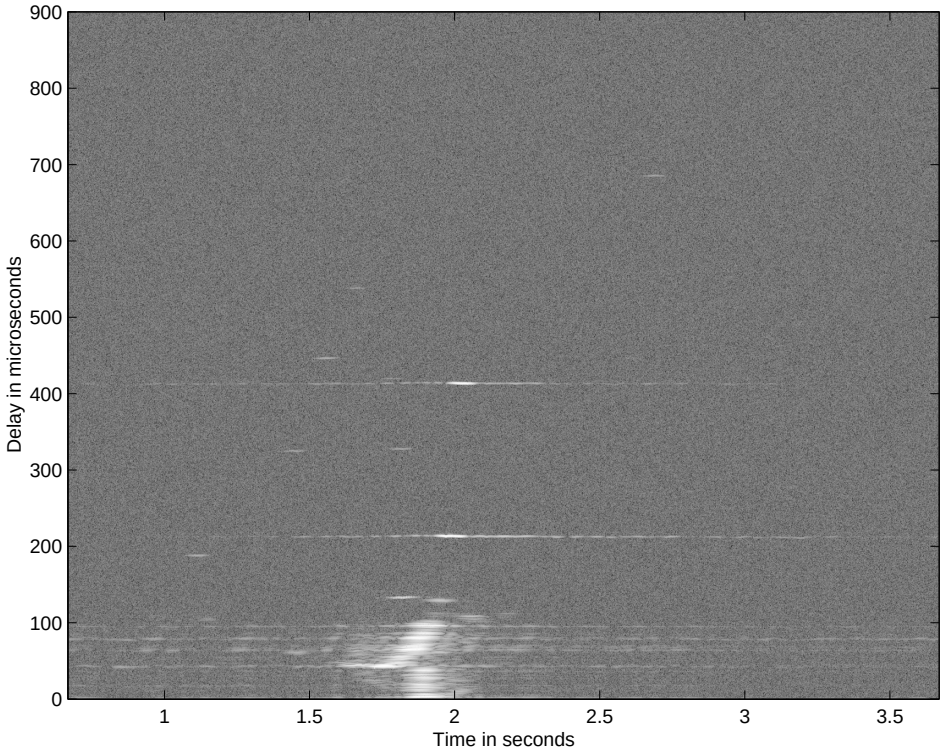

Figure 3.5: The result of improved time alignment by using CFAR.

3.3.1 Algorithm Realization

The modified CLEAN algorithm [17] is realized as follows:

1. Establish a clean image $C(r_m, \theta_n)$: build a blank image field with all pixels set equal to zero;

2. Initialize the residual dirty image: k=1, $R^1(r_m, \theta_n) = P(r_m, \theta_n)$;

3. Find the peak (brightest pixel): $M, N = \arg\max_{m,n} |R^k(r_m, \theta_n)|$;

4. If this peak is really from a complete beampattern, add the location of the peak to the clean image by setting the corresponding pixel to one, then continue; otherwise, go to 8.

5. Form residue vector around the neighborhood of the peak: $\boldsymbol{p} = \text{vec}\{R_k(r_m, \theta_n)\}, \forall (m, n) \in \mathcal{N}\{(M, N)\}$, where $\mathcal{N}\{(M, N)\}$ is large enough to contain a full beampattern.

6. Find the least squares fit to the residual peak for a shifted, scaled, 2-D beam response:

$$\alpha_{opt} = \arg\min_{\alpha,\delta_r,\delta_\theta} \|\boldsymbol{p} - \alpha\hat{\boldsymbol{p}}(\delta_r, \delta_\theta)\|^2$$
$$\hat{\boldsymbol{p}}(\delta_r, \delta_\theta) = \text{vec}\{b_r(r_m - r_M - \delta_r) \times b_\theta(\theta_n - \theta_N - \delta_\theta)\}, \forall(m,n) \in \mathcal{N}\{(M,N)\}$$
$$\alpha_{opt} = \frac{\boldsymbol{p}^H\boldsymbol{p}}{\hat{\boldsymbol{p}}^H\hat{\boldsymbol{p}}}$$

7. Remove the peak from residual: $R^{k+1}(r_m, \theta_n) = R^k(r_m, \theta_n) - \alpha_{opt}\hat{\boldsymbol{p}}$;

8. If the residual magnitude drops below the threshold, such that $\max_{m,n}|R^k(r_m, \theta_n)| < T_0$, done; otherwise, k = k+1, go to 3.

The main modifications from the original CLEAN algorithm are in the form of a scaling parameter α_{opt} and choosing the area to be cleaned. Here we use a least squares fit to find the optimum scaling which matches the estimated beampattern model $\hat{\boldsymbol{p}}$ to the dirty beam $\boldsymbol{p}$. Compared with the standard CLEAN algorithm, which just takes the peak of the dirty image as the position of the next CLEAN component, the modified algorithm carefully chooses the area to be cleaned. This is because with an approximated dirty beam model, some peak brightness feature may be just a region of residual overlapping sidelobes plus noise instead of a complete beampattern.

The process of adding to the CLEAN image and subtracting from the dirty image is cyclically repeated. It is subject to the constraint that when the peak is lower than the noise floor, the process is stopped and the CLEAN image is considered to be complete. This leads to a problem of selecting the threshold T_0. If the threshold is set too high, we will not be able to detect all the echoes. If it is too low, the probability of false alarm, P_{FA}, will increase dramatically. The proposed radar detection with threshold setting scheme is as follows:

Assume that a received signal is represented as

$$R = S + N,$$

where N is random noise, and S is a random variable indicating the presence or absence of some target. The two hypotheses can now be described as

$$H_0 : \text{target is absent: } S < T_0,$$
$$H_1 : \text{target is present: } S \geq T_0.$$

Based upon the observation x, we must make a decision regarding which hypothesis to accept. We divide the entire space, $\mathcal{X}$, into two disjoint regions, $\mathcal{R}$ and $\mathcal{A}$, with $\mathcal{X} = \mathcal{R} \cup \mathcal{A}$. We formulate our decision function $\phi(x)$ as

$$\phi(x) = \begin{cases} 1, & \text{if } x \in \mathcal{R}, \\ 0, & \text{if } x \in \mathcal{A}. \end{cases} \tag{3.1}$$

We interpret this decision rule as follows [18]: If $x \in \mathcal{R}$ (reject) we take action δ_1 (accepting H_1, rejecting H_0); and if $x \in \mathcal{A}$ (accept) we take action δ_0 (accepting H_0, rejecting H_1). The probability of rejecting the null hypothesis H_0 when it is true is called the false alarm probability. For the simple binary hypothesis test,

$$\begin{aligned} \alpha &= P[\text{decide } H_1 | H_0 \text{ is true}] \\ &= P_{FA}, \end{aligned}$$

We will set the threshold T_0 by using an acceptable false alarm rate P_{FA}: choose T_0 such that

$$\int_{T_0}^{\infty} f(x|H_0)\, dx = P_{FA}. \tag{3.2}$$

Here $f(x|H_0)$ follows a Rayleigh distribution because we assume x is the square root of the output y[n] of the complex I-Q matched filter of Figure 3.2. Here we use 10^{-7} as a false alarm rate, which represents the number of false alarm pixels over the total pixels number of the delay-azimuth plot.

3.3.2 Experimental Result

Figure 3.6 shows the CLEAN algorithm result on the same data set as Figure 3.5. Here the stars represent the isolated echoes which the modified CLEAN algorithm detects. It correctly locates the mainlobe position from the severely sidelobe-contaminated point-spread beampattern. Notice that in this operation, we ignore the first strong echo band in the bottom of the plot.

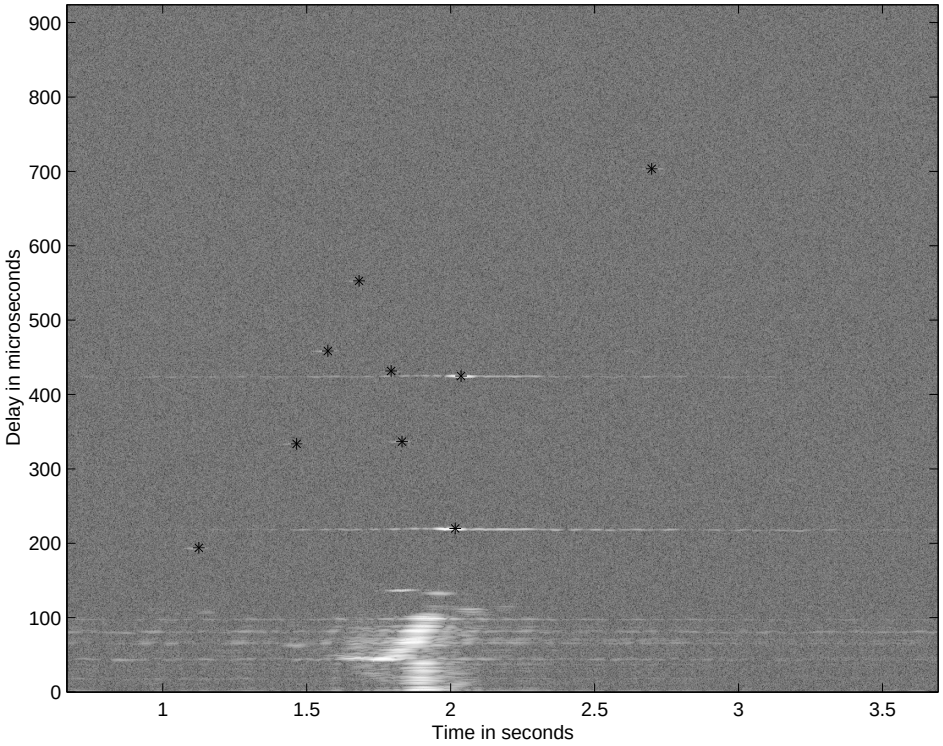

Figure 3.6: The result of the CLEAN algorithm, where the stars represent the echoes which the CLEAN algorithm detects.

3.4 Conclusions

Figure 3.7 shows a hand-made plot of the echoes in five snapshots from the observations of Dr. Fisher. Our experiment with the real data demonstrates that

two apparent echoes inside the rectangles are miss detected by the CLEAN algorithm with constant threshold T_0 derived by Equation 3.2 because of their weak magnitude.

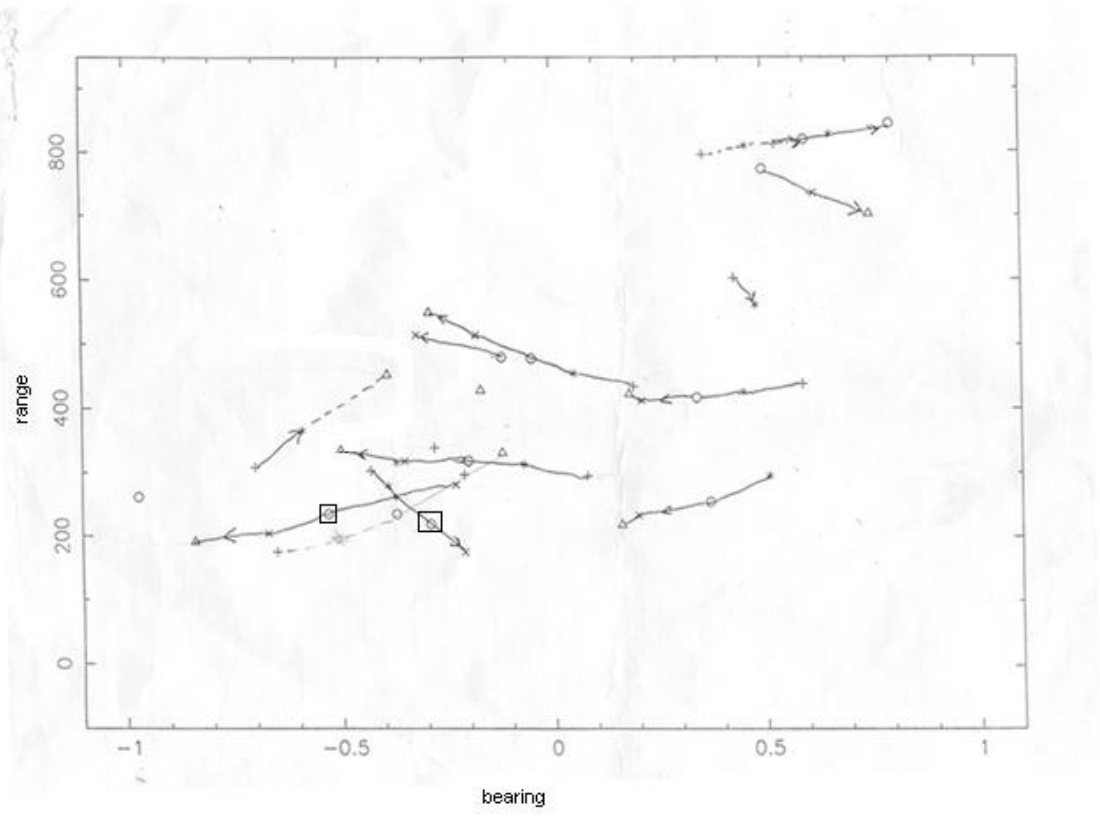

Figure 3.7: The hand-made plot of the echoes in five time intervals by Dr. Fisher. Note that two weaker aircraft echoes, indicated by the square boxes, are miss detected by the CLEAN algorithm with constant threshold T_0.

Astronomers at the GBT would like to find an "intelligent" way to detect all aircraft echoes and blank them from the spectrum, even if some of them are very weak. This motivates using the tracker to improve echo detection performance. We will introduce Kalman tracking in the next chapter to associate the pulses across antenna sweep intervals and build the tracks. For the area where a pulse will occur

with a higher probability, the threshold should be decreased to detect the weaker pulse.

Chapter 4

Kalman Tracking

The Kalman filter theory published in 1960 significantly boosted the development of sophisticated digital filter algorithms for tracking aircraft, artillery shells, submarines and space vehicles. As a result, tracking of objects based on Kalman filter theory has become an established technique of fundamental importance in many engineering applications and scientific investigations. With a Kalman filter it is possible to use the noisy measurements obtained by a track-while-scan RADAR sensor.

From the preceding chapter, we can see that the conventional CLEAN algorithm has limitations in locating weaker aircraft echoes. In this chapter, we will try to estimate the position and velocity of the aircraft with the noisy measurements in range r and bearing θ by introducing an extended Kalman filter. In Chapter 5, we will discuss how this track information can be exploited to derive a prior probability distribution for the pulse to improve the performance of pulse detection in a Bayesian framework.

4.1 Model Selection

Consider an aircraft or similar space vehicle moving with constant velocity perturbed by a zero mean random acceleration. The position of the vehicle is assumed to be measured by range r and bearing θ obtained by a two-dimensional track-while-scan radar sensor. The problem is to obtain the optimum estimates of position and velocity of the vehicle, which leads to a discrete-time two-dimensional, two-state tracking filter.

The measurements obtained at discrete intervals of time of T seconds are assumed to be corrupted with both range and angular noise. The tracking operation is assumed to be performed in the Cartesian coordinate system. In this case, the measurements will not be a linear function of the state. So we will employ extended Kalman filtering for this tracking problem.

4.1.1 Dynamic Model

For each coordinate x and y, aircraft dynamics at snapshot n can be described as [19]

$$x_{n+1} = x_n + \dot{x}_n T + \frac{1}{2} a_n T^2, \tag{4.1}$$

$$\dot{x}_{n+1} = \dot{x}_n + a_n T, \tag{4.2}$$

where

x_n = aircraft position at snapshot n,

$\dot{x}_n$ = aircraft velocity at snapshot n,

a_n = acceleration acting on the aircraft at snapshot n,

T = interval between observations.

In this problem, we will choose as states the position and velocity of the aircraft in the x and y directions. Thus, the proposed states are given by

$$\boldsymbol{X}_n^T = \begin{bmatrix} x_n & y_n & \dot{x}_n & \dot{y}_n \end{bmatrix} \tag{4.3}$$

Therefore, the aircraft dynamics may be represented by a vector-matrix equation of the form

$$\boldsymbol{X}_{n+1} = \boldsymbol{F}\boldsymbol{X}_n + \boldsymbol{G}\boldsymbol{a}_{\boldsymbol{n}}, \tag{4.4}$$

where

$$\boldsymbol{F} = \begin{bmatrix} 1 & 0 & T & 0 \\ 0 & 1 & 0 & T \\ 0 & 0 & 1 & 0 \\ 0 & 0 & 0 & 1 \end{bmatrix}, \tag{4.5}$$

and

$$\boldsymbol{G} = \begin{bmatrix} \frac{T^2}{2} & 0 \\ 0 & \frac{T^2}{2} \\ T & 0 \\ 0 & T \end{bmatrix}, \tag{4.6}$$

$\boldsymbol{X}_n$ is the aircraft state vector, $\boldsymbol{F}$ is the transition matrix, and $\boldsymbol{G}$ is the input distribution matrix.

4.1.2 Measurement Model

Here the nonlinear relation between the quantities measured by the radar and the Cartesian coordinate system selected for tracking operation is explicitly considered. When the measurement equations are nonlinear polar functions of the state, the measurement model is given in [20] by

$$\boldsymbol{Z}_n = \boldsymbol{h}(\boldsymbol{X}_n) + \boldsymbol{V}_n, \tag{4.7}$$

where

$$\boldsymbol{Z}_n = \begin{bmatrix} r_n \\ \theta_n \end{bmatrix}, \tag{4.8}$$

$$\boldsymbol{h}(\boldsymbol{X}_n) = \begin{bmatrix} \sqrt{x_n^2 + y_n^2} \\ \tan^{-1} \frac{y_n}{x_n} \end{bmatrix}, \tag{4.9}$$

$$\boldsymbol{V}_n = \begin{bmatrix} v_r(n) \\ v_\theta(n) \end{bmatrix}, \tag{4.10}$$

r_n = measured range r at snapshot n,

θ_n = measured bearing θ at snapshot n,

$v_r(n)$ = random noise on range r measurement at snapshot n, and

$v_\theta(n)$ = random noise on bearing θ measurement at snapshot n.

4.2 Kalman Tracking Equation

There are two steps for the tracking problem. The first one is a time update step which computes the predictions. The second one is a propagation step which includes computing Kalman gain and measurement update.

4.2.1 Prediction Equation

Since the dynamic model equation is a linear function of the state, then we can still use the traditional prediction equation with initial conditions $\hat{\boldsymbol{X}}(0|0)$ and $\boldsymbol{P}(0|0)$:

$$\begin{aligned} \hat{\boldsymbol{X}}(n+1|n) &= \boldsymbol{F}\hat{\boldsymbol{X}}(n|n), \\ \boldsymbol{P}(n+1|n) &= \boldsymbol{F}\boldsymbol{P}(n|n)\boldsymbol{F} + \boldsymbol{G}\boldsymbol{Q}(n)\boldsymbol{G}, \end{aligned} \tag{4.11}$$

where

$\hat{\boldsymbol{X}}(n|n)$ = filtered state estimate at t_n given data through t_n,

$\tilde{\boldsymbol{X}}(n|n) = \boldsymbol{X}(n|n) - \hat{\boldsymbol{X}}(n|n)$, filtered state estimate error at t_n,

$\boldsymbol{P}(n|n) = E\{\tilde{\boldsymbol{X}}(n|n)\tilde{\boldsymbol{X}}^T(n|n)\}$, filtered state error covariance at t_n,

$\hat{\boldsymbol{X}}(n+1|n)$ = predicted state estimate at t_{n+1} given data through t_n,

$\boldsymbol{P}(n+1|n) = E\{\tilde{\boldsymbol{X}}(n+1|n)\tilde{\boldsymbol{X}}^T(n+1|n)\}$, predicted state error covariance at t_{n+1},

$\boldsymbol{F}$ = discrete state transition matrix,

$\boldsymbol{G}$ = input distribution matrix,

$\boldsymbol{Q}(n)$ = discrete process noise covariance matrix.

4.2.2 Filter Equation

Because the states have been chosen to be Cartesian, the radar measurements r and θ will automatically be nonlinear function of those states. Therefore, a linearized measurement equation can be described as [20]

$$\begin{bmatrix} \Delta r^{\star} \\ \Delta \theta^{\star} \end{bmatrix} = \begin{bmatrix} \frac{\partial r}{\partial x_T} & \frac{\partial r}{\partial y_T} & \frac{\partial r}{\partial \dot{x}_T} & \frac{\partial r}{\partial \dot{y}_T} \\ \frac{\partial \theta}{\partial x_T} & \frac{\partial \theta}{\partial y_T} & \frac{\partial \theta}{\partial \dot{x}T} & \frac{\partial \theta}{\partial \dot{y}T} \end{bmatrix} \begin{bmatrix} \Delta x_T \\ \Delta y_T \\ \Delta \dot{x}_T \\ \Delta \dot{y}_T \end{bmatrix} + \begin{bmatrix} v_r \\ v_\theta \end{bmatrix}, \tag{4.12}$$

where v_θ and v_r represent the measurement noise on angle and range, respectively.

Here we define the measurement sensitivity matrix used in calculating the weighing matrix and the updated covariance as

$$\begin{aligned} \boldsymbol{H} &\triangleq \left[\frac{\partial h}{\partial \boldsymbol{X}}\right]_{\boldsymbol{X}=\hat{\boldsymbol{X}}(n+1|n)} \\ &= \begin{bmatrix} \frac{\partial r}{\partial x(n+1|n)} & \frac{\partial r}{\partial y(n+1|n)} & \frac{\partial r}{\partial \dot{x}(n+1|n)} & \frac{\partial r}{\partial \dot{y}(n+1|n)} \\ \frac{\partial \theta}{\partial x(n+1|n)} & \frac{\partial \theta}{\partial y(n+1|n)} & \frac{\partial \theta}{\partial \dot{x}(n+1|n)} & \frac{\partial \theta}{\partial \dot{y}(n+1|n)} \end{bmatrix} \\ &= \begin{bmatrix} \frac{x(n+1|n)}{\sqrt{x^2(n+1|n)+y^2(n+1|n)}} & \frac{y(n+1|n)}{\sqrt{x^2(n+1|n)+y^2(n+1|n)}} & 0 & 0 \\ \frac{-y(n+1|n)}{\sqrt{x^2(n+1|n)+y^2(n+1|n)}} & \frac{x(n+1|n)}{\sqrt{x^2(n+1|n)+y^2(n+1|n)}} & 0 & 0 \end{bmatrix}. \end{aligned} \tag{4.13}$$

So the filter equations are given by:

$$\begin{aligned} \hat{\boldsymbol{X}}(n+1|n+1) &= \hat{\boldsymbol{X}}(n+1|n) + \boldsymbol{K}(n+1)\Big[\boldsymbol{z}(n+1) - \boldsymbol{h}\Big(\hat{\boldsymbol{X}}(n+1|n), t_{n+1}\Big)\Big], \\ \boldsymbol{P}(n+1|n+1) &= \Big[\boldsymbol{I} - \boldsymbol{K}(n+1)\boldsymbol{H}(n+1)\Big]\boldsymbol{P}(n+1|n), \\ K(n+1) &= \boldsymbol{P}(n+1|n)\boldsymbol{H}^T(n+1)\big[\boldsymbol{H}(n+1)\boldsymbol{P}(n+1|n)\boldsymbol{H}_T + \boldsymbol{R}(n+1)\big]^{-1}, \end{aligned} \tag{4.14}$$

where

$$\begin{aligned}
\boldsymbol{z}(n+1) &= \text{vector of measurements at } t_{n+1},\\
\boldsymbol{h}(\boldsymbol{X}, t) &= \text{vector of measurement model equations},\\
\boldsymbol{h}\Big(\hat{\boldsymbol{X}}(n+1|n), t_{n+1}\Big) &= \text{vector of predicted measurements at } t_{n+1},\\
\boldsymbol{H}(n+1) &= \left[\frac{\partial h(\boldsymbol{X}, t)}{\partial \boldsymbol{X}}\right]_{\boldsymbol{X}=\hat{\boldsymbol{X}}(n+1|n), t=t_{n+1}},\\
\boldsymbol{R}(n+1) &= \text{measurement noise covariance matrix at } t_{n+1},\\
\boldsymbol{K}(n+1) &= \text{Kalman filter gain matrix at } t_{n+1}.
\end{aligned}$$

4.3 Parameter Selection

The appropriate selection of process noise covariance matrix $\boldsymbol{Q}$ and the measurement noise covariance matrix $\boldsymbol{R}$ are important for the design of Kalman tracker. In this section, we will describe the selection of these two parameters when we build the Kalman trackers for GBT Radar Data.

4.3.1 Process Noise Covariance Matrix Q

The statistical model of the signal process is assumed to be described by a linear vector-matrix equation of the form

$$\boldsymbol{X}_{n+1} = \boldsymbol{F}\boldsymbol{X}_n + \boldsymbol{G}\boldsymbol{a}_{\boldsymbol{n}},$$

where

$$\boldsymbol{a}_{\boldsymbol{n}} = \begin{bmatrix} a_x(n) \\ a_y(n) \end{bmatrix},$$

and $\boldsymbol{Q}$ is the covariance matrix of the process noise $\boldsymbol{a}_{\boldsymbol{n}}$.

Here we will discuss two kinds of maneuver models: a white noise maneuver model and a colored noise maneuver model. There are three assumptions for the white noise maneuver model:

1. Acceleration values at different snapshots are assumed to be uncorrelated.

2. The random acceleration is assumed to be of equal variance and also independent along both the x and y axes.

3. The acceleration along the x and y axes is assumed a random constant across successive scans with zero mean and constant variance σ_a^2.

In this case,

$$E\{a_x\} = 0,$$
$$E\{a_y\} = 0,$$
$$E\{a_x a_y^T\} = \boldsymbol{Q} = \begin{bmatrix} \sigma_a^2 & 0 \\ 0 & \sigma_a^2 \end{bmatrix}. \tag{4.15}$$

In a practical scenario, the movement of the aircraft generated by the white noise maneuver model is not smooth enough to model commercial aircraft trajectories. To smooth the movement, we introduce the colored noise maneuver model, which can be easily generated by passing the white noise through a FIR low-pass filter. So the plant noise $\boldsymbol{Q}$ can be expressed as:

$$\boldsymbol{Q} = E\{a_x a_y\} = \begin{bmatrix} \sigma_x^2(n) & \sigma_{xy}^2(n) \\ \sigma_{xy}^2(n) & \sigma_y^2(n) \end{bmatrix}. \tag{4.16}$$

4.3.2 Measurement Noise Covariance Matrix R

The statistical model of the measurement process is assumed to be described by

$$\boldsymbol{Z}_n = \boldsymbol{h}(\boldsymbol{X}_n) + \boldsymbol{V}_n,$$

where

$$\boldsymbol{V}_n = \begin{bmatrix} v_r(n) \\ v_\theta(n) \end{bmatrix}.$$

$\boldsymbol{R}$ is the covariance matrix of the measurement noise $\boldsymbol{V}_n$.

It is assumed that the measurement noise for r and bearing θ are independent white Gaussian noise, So $\boldsymbol{R}$ can be expressed as:

$$\boldsymbol{R} = \begin{bmatrix} \sigma_r^2 & 0 \\ 0 & \sigma_\theta^2 \end{bmatrix} \tag{4.17}$$

4.4 Track Management

For multi-target tracking, track management such as track association, track dropping and the strategy for cases when some measurements are missed or some new tracks are created, is very critical to tracking performance. This section introduces the approach used in each of these cases.

4.4.1 Track Association

Kalman tracking consists of two phases: prediction and update. For a single tracker, after getting a new prediction $\hat{\boldsymbol{X}}_{n+1|n}$, we need the following rules to associate this prediction with the possible measurements around it.

We will define an elliptical region for each track inside of which we will probably find the next snapshot detection measurement associated with the prediction. Only detections within the ellipse may be associated with the given track. The origin of the ellipse is the prediction point $(\hat{x}_{n+1|n}, \hat{y}_{n+1|n})$, and the radii are a factor multiplied by $\sqrt{\boldsymbol{P}_{n+1|n}(1,1)}$ and $\sqrt{\boldsymbol{P}_{n+1|n}(2,2)}$, where $\boldsymbol{P}_{n+1|n}$ is the estimation error covariance matrix before processing the measurement.

It is possible that there are several candidate measurements around the prediction point inside the elliptical region, whose amplitudes are higher than the proposed threshold. The rule is to choose at most two echoes which have the higher amplitudes as the measurements to continue the update phase.

4.4.2 Some Measurements Missed

Sometimes when the echo is so weak that we cannot find any detection around the prediction, then it is probably that some measurement is missed at that snapshot. We will have to make a two-step prediction and try to find measurement around that new prediction in the succeeding snapshot. As a result, the prediction equation for time interval $2T$ are given by:

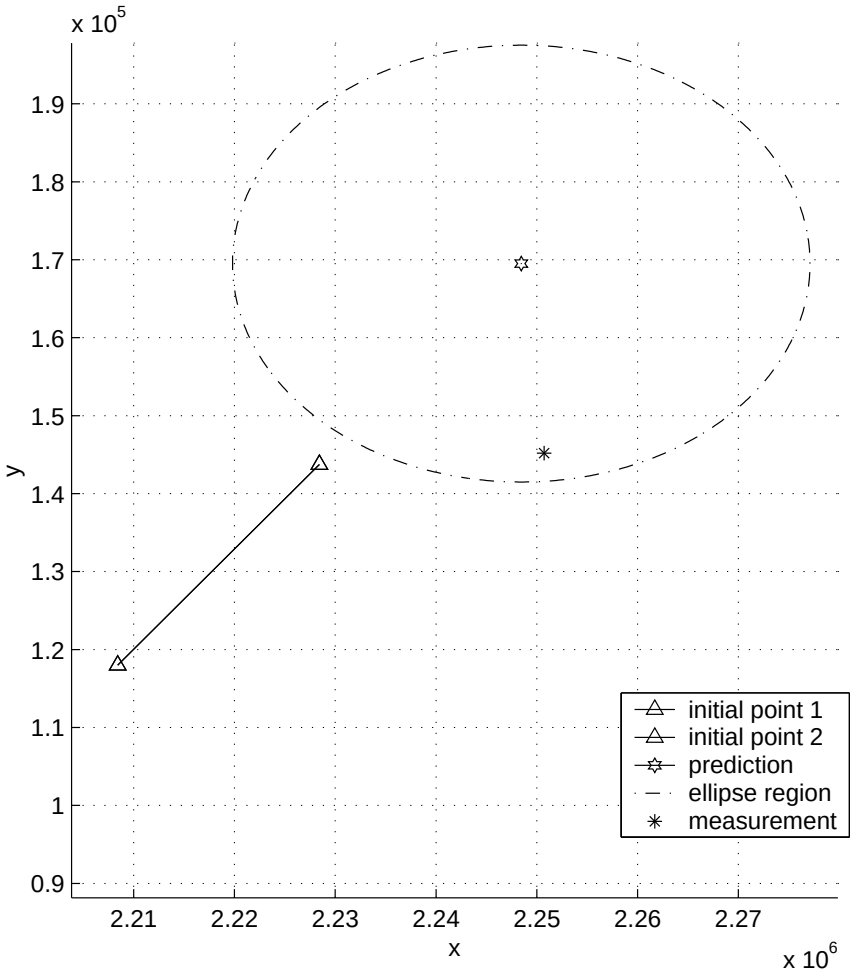

Figure 4.1: The ellipse region around the prediction.

$$\hat{\boldsymbol{X}}(n+2|n) = \boldsymbol{F}\hat{\boldsymbol{X}}(n|n)$$
$$\boldsymbol{P}(n+2|n) = \boldsymbol{F}\boldsymbol{P}(n|n)\boldsymbol{F} + \boldsymbol{G}\boldsymbol{Q}(n)\boldsymbol{G}$$

where

$$\boldsymbol{F} = \begin{bmatrix} 1 & 0 & 2T & 0 \\ 0 & 1 & 0 & 2T \\ 0 & 0 & 1 & 0 \\ 0 & 0 & 0 & 1 \end{bmatrix} \tag{4.18}$$

and

$$\boldsymbol{G} = \begin{bmatrix} \frac{(2T)^2}{2} & 0 \\ 0 & \frac{(2T)^2}{2} \\ 2T & 0 \\ 0 & 2T \end{bmatrix} \tag{4.19}$$

The size of the ellipse region will also increase as the time interval changes from T to $2\,T$. The time interval could also keep increasing to $3\,T$, if there is one more detection missed. Figure 4.2 shows the kalman tracking for two-step prediction.

4.4.3 Dropping a Track

If there are more than three measurements continuously missed, we assume that this track is not reliable, so it has to be dropped. Figure 4.3 shows that a track will be dropped from a track list and will receive no new associations after successively missing three detections in a row.

4.4.4 Creating a New Track

At each snapshot, it is possible to create some new tracks in addition to continuing the existing tracks. Figure 4.4 shows that a new track is created in the second snapshot, which locates in the bottom right part of the figure. This feature guarantees that the tracking system can automatically find new tracks in every snapshot.

4.4.5 Splitting a Track

Sometimes it is possible to find more than one detection following the existing tracks at a measurement. In this case, the track will be split. We will then track these split tracks respectively. Figure 4.4 also shows that some splits can happen in some snapshots.

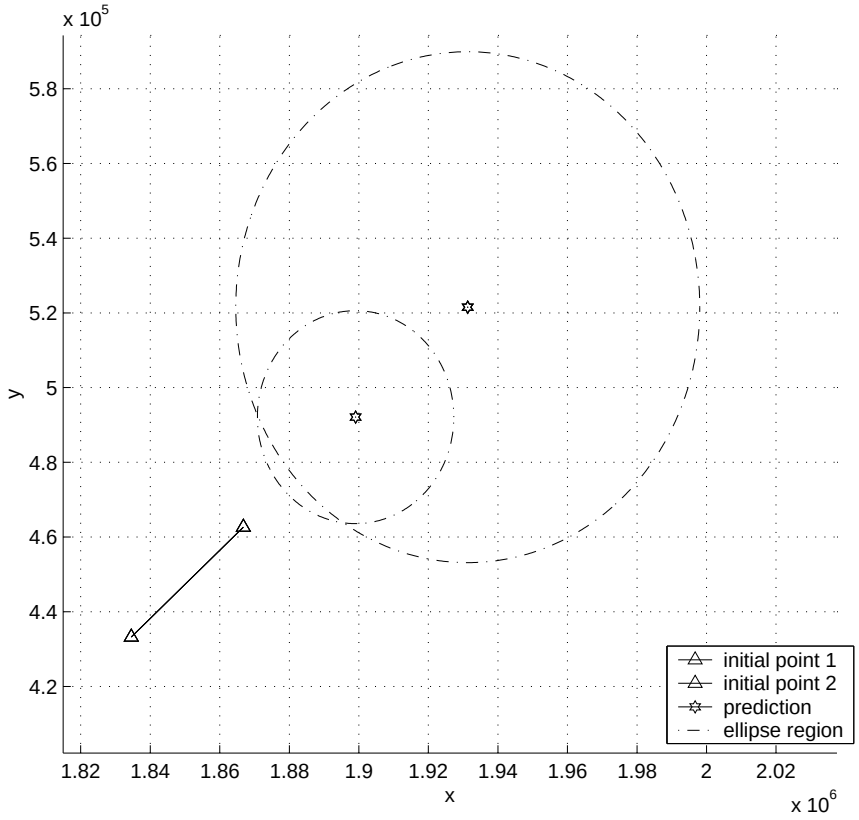

Figure 4.2: Two-step prediction and the corresponding increased elliptical region.

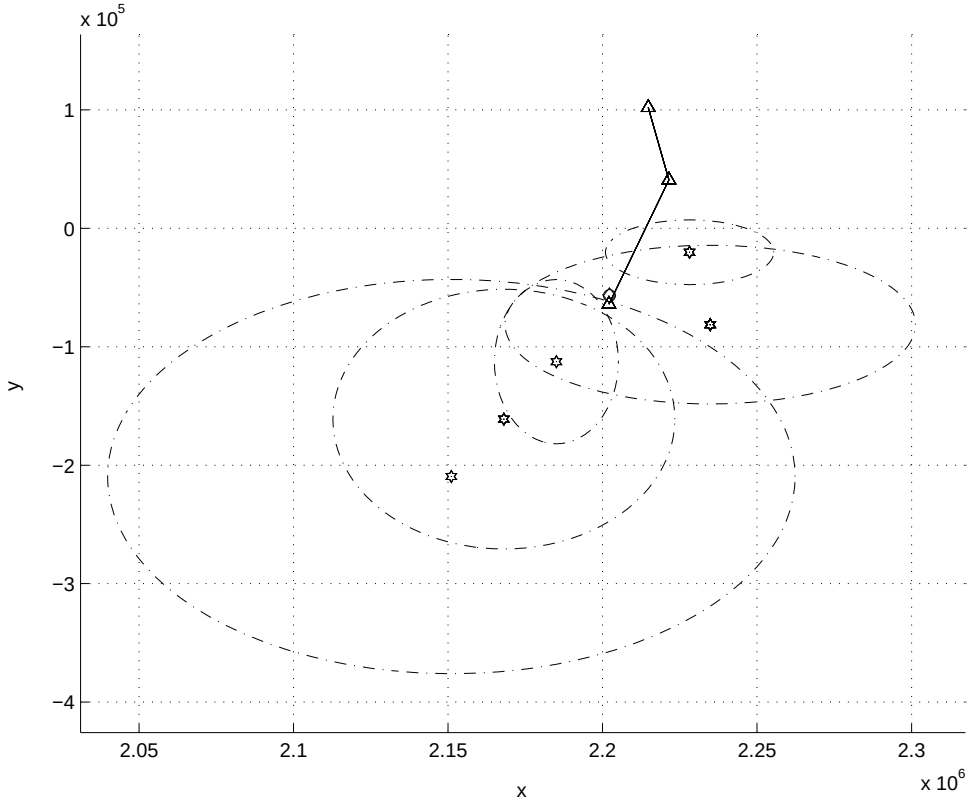

Figure 4.3: A track is dropped after continuously missing 3 detections.

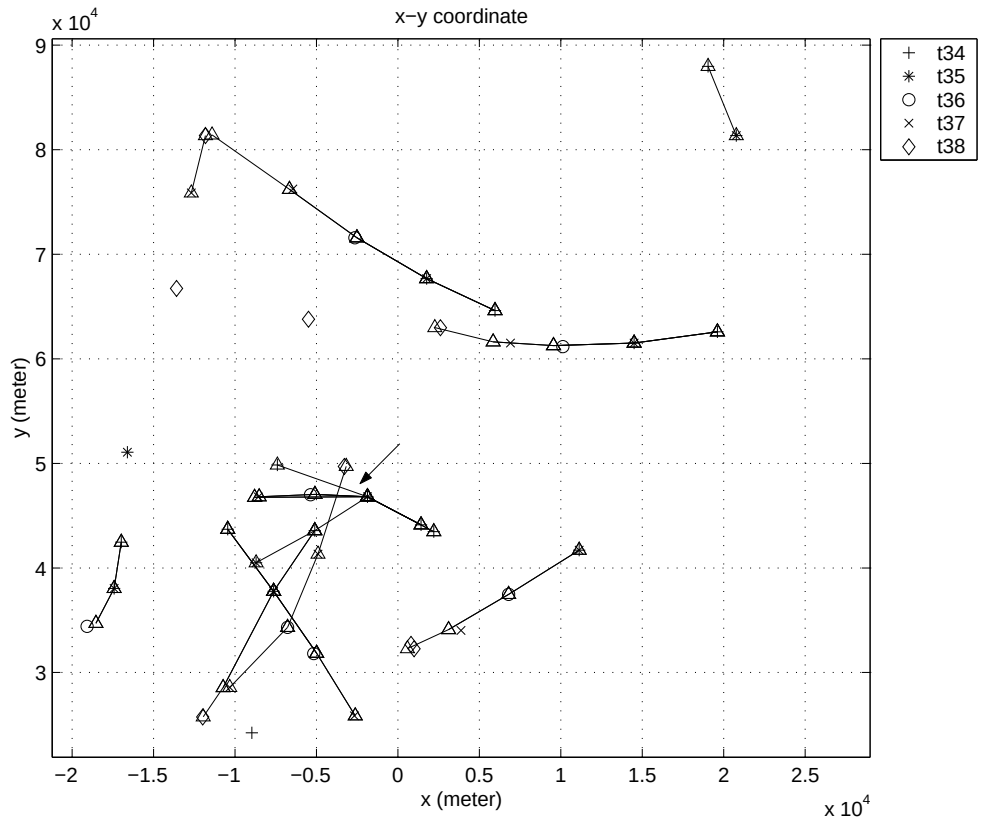

Figure 4.4: Kalman tracking for five snapshots. Note the track split that occurs near the arrow.

Chapter 5

A Proposed Bayesian Combined tracking With Detection Algorithm

In this chapter, we focus on developing a Bayesian algorithm to help the performance of echo detection by using the Kalman tracker to provide a prior probability distribution for the pulses. We will discuss two modes here: real-time processing and post processing.

5.1 Real-Time Processing

Assume we have k data files, D_1 to D_k, recorded at time indices $t_1, t_2, ..., t_k$. The scheme for real-time processing mode at time index t_n is as follows:

1. Build the track prediction for aircraft motion at t_n using time-history detection information from previous data files D_1 to D_{n-1};

2. Blank the data in the prediction regions found in step 1;

3. Compute the prior probability distribution of the pulses at t_n and incorporate this prior distribution model to calculate detection thresholds;

4. Detect the pulses with the proposed threshold and use the CLEAN algorithm to locate positions for isolated echo points in D_n. This step prepares track information for the next run;

5. if $n < k$, then $n = n + 1$; Go to step 1.

5.1.1 Pulse Arrival Prior Distribution

Given the position information for pulses from data files D_1 to D_n, we can use Kalman tracking to find a prediction point $(\hat{x}_{n+1|n}, \hat{y}_{n+1|n})$ where a detection is expected at time t_{n+1}. In section 4.4.1, we defined an elliptical region $\mathcal{S}$ with the prediction point as the centroid and radii r_x and r_y proportional to $\sqrt{\boldsymbol{P}_{n+1|n}(1,1)}$ and $\sqrt{\boldsymbol{P}_{n+1|n}(2,2)}$ respectively, where $\boldsymbol{P}_{n+1|n}$ is the estimation error covariance matrix before processing the measurement. Next we will establish a prior probability distribution model over that elliptical region.

We define the probability density model for the occurrence of an echo over the elliptical region as a two-dimensional Gaussian distribution in a truncated elliptical area, $\mathcal{S}$, as follows:

$$f(x,y) = \begin{cases} \frac{1}{2\pi\sigma_x\sigma_y} e^{-\frac{1}{2}[\frac{(x-\hat{x}_{n+1|n})^2}{\sigma_x^2} + \frac{(y-\hat{y}_{n+1|n})^2}{\sigma_y^2}]}, & \text{if } (x,y) \in \mathcal{S}; \\ \frac{1-P_{\mathcal{S}}}{|\Omega|-|\mathcal{S}|}, & \text{if } (x,y) \in \bar{\mathcal{S}}. \end{cases} \tag{5.1}$$

where

$$\mathcal{S} : \frac{(x-\hat{x}_{n+1|n})^2}{r_x^2} + \frac{(y-\hat{y}_{n+1|n})^2}{r_y^2} \leq 1 \text{ and } \mathcal{S} \cup \bar{\mathcal{S}} = \Omega;$$

$$P_{\mathcal{S}} = \iint_S f(x,y)\, dS, (x,y) \in \mathcal{S};$$

$$|\Omega| = \iint_\Omega dxdy, (x,y) \in \Omega;$$

$$|\mathcal{S}| = \iint_S dxdy, (x,y) \in \mathcal{S}.$$

This model assumes that a given track leads to the presence with probability one of one echo occurring somewhere in the field, Ω, at t_{n+1} . Outside of $\mathcal{S}$, there is a low constant probability density. Near the prediction point, the probability increases. This model is an arbitrary but reasonable practical choice because it satisfies the following characteristics needed for the proposed f(x,y):

- The prior probability of the presence of an echo decreases as the distance from the centroid increases.

- The distribution has a smooth shape over $\mathcal{S}$ to guarantee the prior probability derived from it is smoothly changing as a function of distance from the prediction point.

- The shape of the density surface depends on prediction error covariance, $\boldsymbol{P}_{n+1|n}$, such that higher prediction error leads to lower probability density.

To simplify notation , we set

$$\alpha \triangleq \frac{r_x}{r_y} = \frac{\sigma_x}{\sigma_y}, \tag{5.2}$$

so that α determines the shape of the elliptical region $\mathcal{S}$. We also move the centroid of the ellipse, $(\hat{x}_{n+1|n}, \hat{y}_{n+1|n})$, to (0,0). This will not affect the calculation of prior probability later. Using (5.2), we can simplify (5.1) as:

$$f(x,y) = \begin{cases} \frac{1}{2\pi\alpha\sigma_y^2} e^{-\frac{1}{2}[\frac{x^2}{\alpha^2\sigma_y^2} + \frac{y^2}{\sigma_y^2}]}, & \text{if } (x,y) \in \mathcal{S}; \\ \frac{1-P_{\mathcal{S}}}{|\Omega|-|\mathcal{S}|}, & \text{if } (x,y) \in \bar{\mathcal{S}}. \end{cases} \tag{5.3}$$

Figure 5.1 shows this density function f(x,y) for $\alpha = 0.5$.

As figure 5.2 shows, for any point (x_1, y_1) inside the elliptical region $\mathcal{S}$, we can always fit this point to an ellipse $\mathcal{S}1$ with the following form:

$$\mathcal{S}1 : \frac{x^2}{r_{x_1}^2} + \frac{y^2}{r_{y_1}^2} = 1, \tag{5.4}$$

where r_{x1} and r_{y1} are the radii of the ellipse $\mathcal{S}1$ which satisfy $\frac{r_{x_1}}{r_{y_1}} = \frac{r_x}{r_y} = \alpha$.

Then we define a very small "patch" S_p around a particular point (x_1, y_1) and make the following assumptions about this small area:

- The small "patch" is defined within range and bearing angle resolution scope, $\Delta R \approx 13.8655$ meter and $\Delta\theta \approx 0.0015$ radian. ΔR is the range resolution of the row data determined by time sample spacing. $\Delta\theta$ is the bearing resolution determined by the pulse repetition rate and antenna rotation rate at the RADAR transimitter. So the area for this patch $A \approx 0.0208R$, where R is the range measurement of point (x_1, y_1).

- The probability density function $f(x,y)$ is approximate the same constant inside this patch.

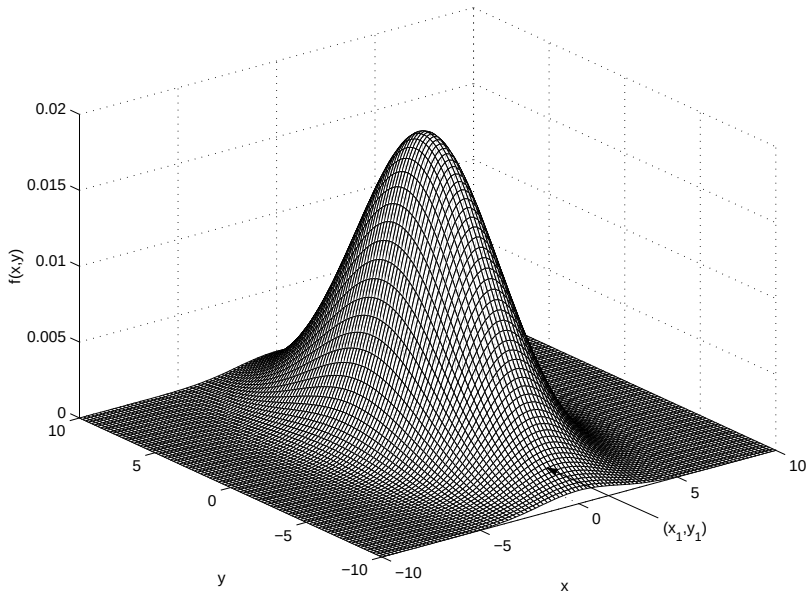

Figure 5.1: Two dimensional Gaussian model over the elliptical region $\mathcal{S}$. Note that (x_1, y_1) is a particular point inside $\mathcal{S}$.

So for a particular point (x_1, y_1), the prior probabilities $P(H_1)$ and $P(H_0)$ where H_1 and H_0 are defined in section 3.3.1 can be described by the piecewise probabilities over S_p as follows:

$$P(H_1) = \iint_{S_p} f(x_1, y_1)\, dS \tag{5.5}$$

$$= A * f(x_1, y_1) \tag{5.6}$$

$$= A * \frac{1}{2\pi\sigma_x\sigma_y} e^{-\frac{1}{2}[\frac{x_1^2}{\sigma_x^2}+\frac{y_1^2}{\sigma_y^2}]}$$

$$= A * \frac{1}{2\pi\alpha\sigma_y^2} e^{-\frac{1}{2}[\frac{x_1^2}{\alpha^2\sigma_y^2}+\frac{y_1^2}{\sigma_y^2}]} \tag{5.7}$$

$$= A * \frac{1}{2\pi\alpha\sigma_y^2} e^{-\frac{r_{y_1}^2}{2\sigma_y^2}}. \tag{5.8}$$

Here (5.7) follows from the fact that $\sigma_x/\sigma_y = r_{x_1}/r_{y_1} = \alpha$, and (5.8) is follows from the fact that (x_1, y_1) satisfies $\frac{x_1^2}{r_{x_1}^2} + \frac{y_1^2}{r_{y_1}^2} = 1$. In (5.8), the area of the patch A in (5.8) will increase as the range R increases, as figure 5.3 shows. But for the same track quality (i.e. no change in $\boldsymbol{P}_{n+1|n}$), an increase in R will lead to the radius of the

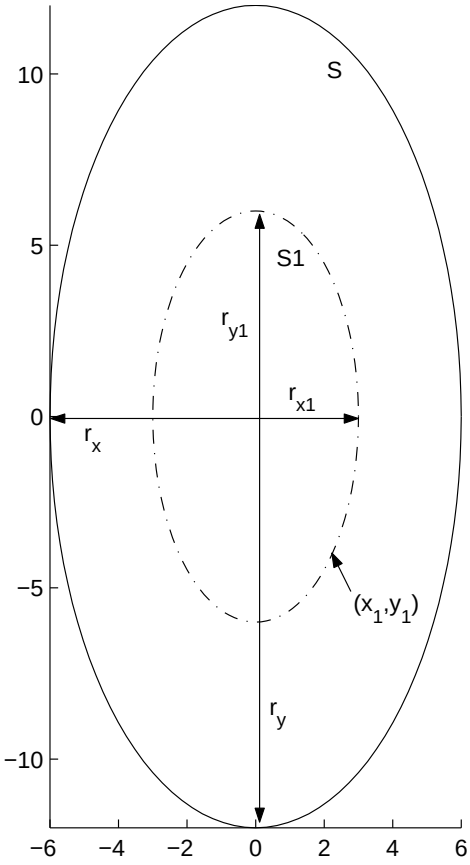

Figure 5.2: Contours of density function $f(x, y)$, where the radii of $\mathcal{S}$ and $\mathcal{S}1$ have the following relationship: $r_x/r_y = r_{x_1}/r_{y_1} = \alpha$.

elliptical region r_y increasing. This will cause a decrease of σ_y (We will mention that σ_y is inversely proportional to r_y later). So the second term of (5.8) will decrease as R increases, which will approximately cancel out the effect of linear relation R in the first term A. Thus $P(H_1)$ is not dependent on range.

Finally, we will have the expression of $P(H_1)$ and $P(H_0)$ as follows:

$$P(H_1) = Ce^{-\frac{r_{y_1}^2}{2\sigma_y^2}}, \tag{5.9}$$

$$\begin{aligned} P(H_0) &= 1 - P(H_1), \\ &= 1 - Ce^{-\frac{r_{y_1}^2}{2\sigma_y^2}}. \end{aligned} \tag{5.10}$$

where C is a constant.

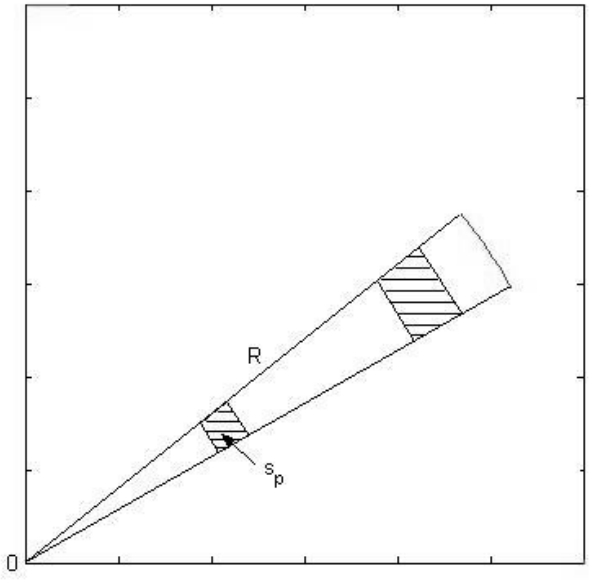

Figure 5.3: The area of patch increases as the range R increases.

To calculate $P(H_1)$ and $P(H_0)$ in (5.9) and (5.10), we must have two parameters: r_{y_1} and σ_y. We define σ_y is to be inversely proportional to r_y, the radius of the elliptical region $\mathcal{S}$ along the y axis. So when the size of the region increases, the density function becomes shorter and wider. This will lead to a smaller decrease in the detection threshold, $T(x, y)$, in the Bayesian detection scheme defined below. We will discuss the reason for this parameter selection in section 5.1.3. In general, r_{y_1} can be seen as a relative "distance" from a point (x_1, y_1) to the prediction point and can be computed by:

$$r_{y_1}^2 = \frac{(x_1 - \hat{x}_{n+1|n})^2}{\alpha^2} + \frac{(y_1 - \hat{y}_{n+1|n})^2}{1^2}, \tag{5.11}$$

where α can be derived by (5.2). We notice that a point closer to the prediction point will have a higher $P(H_1)$ than a point further away.

5.1.2 Threshold Setting for the CLEAN Algorithm

The main idea of the variable threshold for the CLEAN algorithm is that we want to decrease the threshold for the weaker pulses to be detected if they happen to be located in an area where the echo occurs with higher probability. We will now use the prior probability calculated using Kalman tracking information to set a variable threshold for the areas around the prediction points.

But first, we want to clarify the definition of probability of false alarm, P_{FA}, and probability of detection, P_D. They represent the probability of a received signal, x, exceeding a threshold under the hypotheses of the absence, H_0, or presence, H_1, of the echo respectively, as figure 5.4 shows.

By taking into account the true probability of the presence of the echo, P_{H_1}, or the absence of the echo, P_{H_0}, we introduce definitions for total P_{FA} and total P_D as follows:

$$\begin{aligned} P_{TFA} &= \text{total } P_{FA} \\ &\triangleq (P_{H_0})(P_{FA}) \\ &= P(x > T \cap H_0) \\ &= (P_{H_0}) \int_T^\infty f(x|H_0)\, dx, \end{aligned}$$

$$\begin{aligned} P_{TD} &= \text{total } P_D \\ &\triangleq (P_{H_1})(P_D) \\ &= P(x > T \cap H_1) \\ &= (P_{H_1}) \int_T^\infty f(x|H_1)\, dx. \end{aligned} \tag{5.12}$$

These are unconditional probabilities of false alarm and detection respectively. The state, H_0 or H_1, is treated as random, so that we may incorporate our prior model P_{H_0} into the detection scheme as follows:

$$P_{TFA} = \text{constant}, \tag{5.13}$$

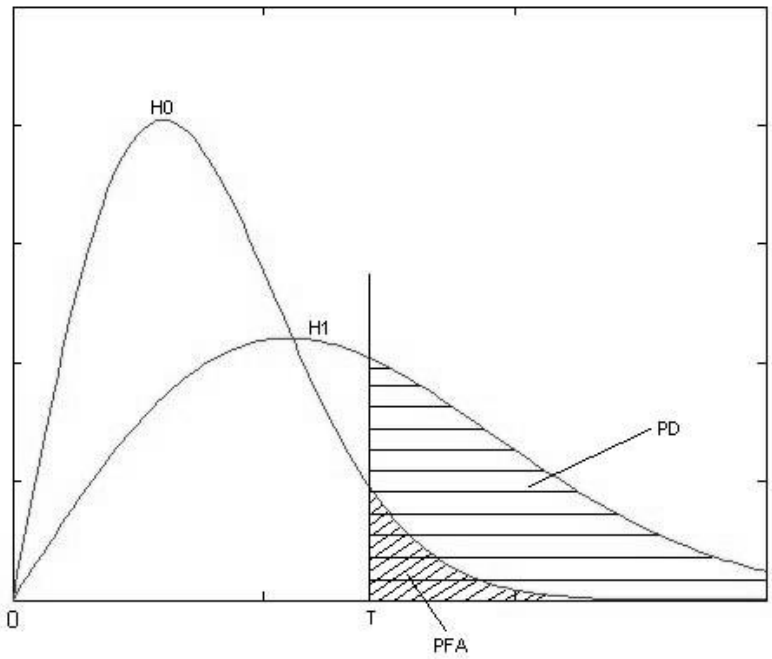

Figure 5.4: P_{FA} and P_D under the two hypotheses: H_0 and H_1.

that is,

$$P_{H_0} \times \int_{T(x,y)}^{\infty} f(x|H_0)\, dx = \text{constant}. \tag{5.14}$$

This constant will be set by design at an acceptably low level, and the corresponding threshold value, $T(x, y)$ wil be computed for each point in the data. Compared with the constant threshold, T_0, discussed in section 3.3.1, $T(x, y)$ is decided by the prior distribution of the presence of pulse: $P_{H_0} = 1 - P_{H_1}$. According to the prior distribution model we discussed, from the edge to the centroid of the elliptical region around the prediction point, $T(x, y)$, decreases as H_0 decreases, in order to keep total P_{FA} as a constant. Compared with the conventional CLEAN algorithm with a constant threshold, by using the decreased threshold in the region where the pulse occurs with higher probability, the weaker pulses will be detected. This occurs without increasing the overall number of false alarms. Figure 5.5 demonstrates the variable threshold $T(x, y)$.

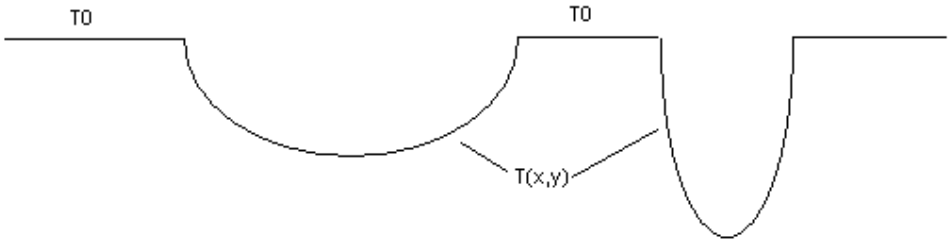

Figure 5.5: The threshold T is decided by the prior distribution of the presence of pulse, where T_0 is the constant threshold outside the elliptical region around the prediction point and the sectional drawings of two concavities represent the decreased threshold $T(x, y)$ according to the prior probability inside the elliptical region.

5.1.3 Tradeoff between Probability of False Alarm and Probability of Detection

This Bayesian Combined tracking with detection Algorithm helps to detect the weaker pulses, but it may pick up some false alarms due to the decreased threshold in the region around the prediction. So if the constant threshold outside the prediction regions is not adjusted up slightly, the new algorithm may have a higher false alarm rate than the old algorithm. There are two criteria for setting the threshold, that is, for parameter selection in the prior distribution model.

- The decreased threshold $T(x, y)$ in the elliptical region around the prediction point should not dramatically increase P_{FA} when it improves P_D. This is achieved by carefully selecting the parameters for $f(x, y)$.

- The decreased threshold $T(x, y)$ is inversely proportional to the size of the elliptical region. This guarantees that P_{FA} will not increase dramatically as the size of elliptical region increases significantly, which usually occurs when some measurements are missed. Figure 5.5 demonstrates that the left concavity has less threshold decrease than the right one because the right elliptical region has smaller size than the left one. This is achieved by setting σ_y in (5.9) to be

inversely proportional to r_y, the radius of the elliptical region $\mathcal{S}$ along the y axis.

5.2 Post Processing

The main difference between post processing and real-time processing modes is that post processing blanks corrupted data after detection, while real-time processing blanks before detection, using only the prediction regions derived from the Kalman tracker.

For post processing, the detection step will identify all the echoes which exceed the threshold set by existing tracker information. Thus the blanking area should be smaller and more accurate than the prediction region for real-time process because actual detections rather than prediction regions are need to define blanking areas. As a result, the post processing mode has better performance than the real-time model.

Chapter 6

Results

In this chapter, we will first demonstrate results for the new Bayesian combined tracking with detection algorithm. When compared with conventional pulse detection, this new algorithm is able to detect weaker aircraft echoes, and thus improves the detection performance significantly. We will demonstrate this improvement for both simulation data and real data from the GBT in real time processing mode. The effect on data spectrum at the GBT when using simple time window blanking, tracked pulse blanking, and Bayesian tracking with detection, will be studied.

6.1 Simulation Data

To evaluate the detection performance improvement of the Bayesian combined tracking with detection algorithm under known, controlled conditions, we can use some simplified data to simulate the real case. Several performance criteria such as probability of detection, P_D, v.s. probability of false alarm, P_{FA}, and P_D v.s. signal-to-noise ratio (SNR) exhibit some improvements when compared with the conventional approach.

6.1.1 Simulation Model

The assumptions for this simplified simulation model are as follows:

- The receiver and antenna follow the same conditions as the real ones in the GBT, so the radar parameters keep as same as in the real ones.

- We use additive white gaussian noise (AWGN) with the variance ${\sigma_\eta}^2$ matching sample variance estimated from real GBT data.

- There is only one simulated echo track in each randomly generated trail observation. The state space model and the measurement model of the aircraft exactly follow the same rule as in the real data case.

- The pulse echo amplitude follows a Swirling distribution IV model for a square law receiver [21]. The radar received pulses have constant amplitude throughout an entire scan, but are uncorrelated from pulse to pulse. The echo amplitude probability density function (pdf) is given by

$$f_\Sigma(\sigma) = \frac{4\sigma}{\sigma_{av}^2} exp(-\frac{2\sigma}{\sigma_{av}}), \tag{6.1}$$

  where σ_{av} denotes the average radar cross section (RCS) over all target fluctuations.

6.1.2 Performance Evaluation and Comparison

In this section, we will use Monte-Carlo simulation for repeated random trials to evaluate P_D v.s. P_{FA} in order to estimate the likelihood ratio statistics and the receiver operating characteristic (ROC). When comparing the two algorithms, we must creafully consider the differences in how false alarms arise by conventional definition:

$$P_{FA} = \int_{T_0}^{\infty} f(x|H_0)\, dx = P(x > T_0|H_0). \tag{6.2}$$

That is, P_{FA} only depends on the noise floor and a fixed threshold. In section 5.1.3, we discussed the new algorithm improves P_D at the cost of a slight increase of P_{FA} due to a position descendant threshold controlled by the tracker. So as to make a fair comparison of detection performance for two algorithms, we have to compare P_D for both algorithms for the same effective total P_{FA} value, by slightly decreasing the constant threshold T_0 for the conventional algorithm to match the increased P_{FA} of the new algorithm.

Figure 6.1 demonstrates the performance improvement of the new algorithm compared with the conventional one for different signal-to-noise ratios (SNRs). From

the plot, we notice that the conventional algorithm achieves the same P_D level in theory by decreasing the constant threshold, but this causes P_{FA} to increase remarkably. The new algorithm can improve P_D without significantly increasing P_{FA}. This controlled experiment suggests that the Bayesian tracking-detection approach is very promising.

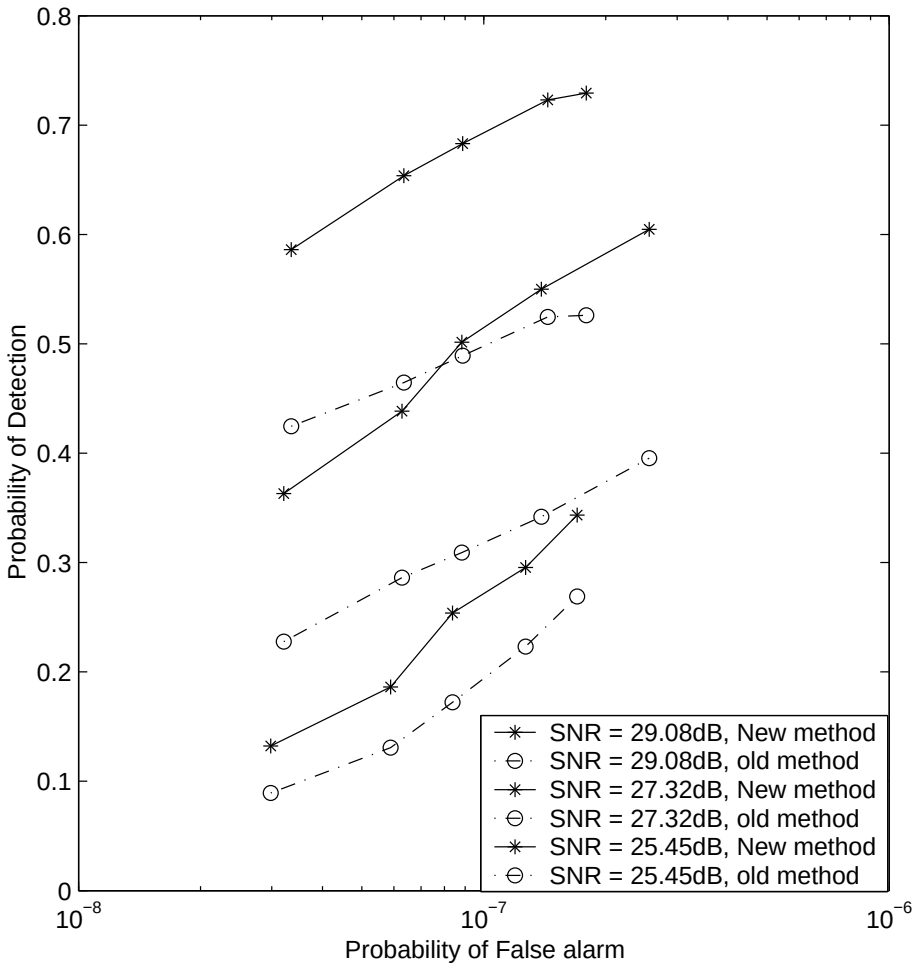

Figure 6.1: P_{FA} v.s. P_D in different SNR for two algorithms: "new" Bayesian combined tracking with detection algorithm and "old" pulse detection algorithm.

6.2 Real Data

Detection would usually not be directly from GBT data, but using a test horn antenna located nearby with some higher gain in the direction of expected echoes (GBT sidelobe response level peaks at about 0 dBi, and the horn antenna has a few dB more gain). This yields higher INR to improve detection, then the detected pulse times would be used to control blanking at the same times in the simultaneously observed GBT high gain antenna data.

Two sets of real data were used to test our algorithms: The first data set was recorded at the GBT the morning of April 5, 2002. The purpose of these data were to look for aircraft passing north of the observatory by taking sample sets one minute apart and looking for echoes that move uniformly in delay and radar antenna azimuth position. The receiving horn was pointed to +5 degrees elevation and indicated azimuth 357 degree. The second one contains continuous 10-minute-data blocks (50 radar rotations) recorded in Jan, 2003 with essentially the same receiver and antenna conditions. The main difference is that the new data rate is 10 Msamp/s, as compared to 10.81818 Msamp/s for data set 1.

6.2.1 Data Set 1

There are five data files in the first data set, which include many pulses from the aircraft. Some of the strong pulses exhibit a prominent transmitter antenna beampattern with the sidelobes covering a wide angle range. Analysis of this data set is valuable for studying of blanking with complex RFI. Here we will detect the echoes in the first two data files, t_{34} and t_{35}, by using the conventional algorithm and use detections to initiate the Kalman tracker. Figure 6.2 shows the pulse delay distribution and the detected echoes for data files t_{34} and t_{35}. Figure 6.3, Figure 6.4 and Figure 6.5 show the process of Kalman tracking and echo detection using both the new and conventional algorithms for the succeeding data files, i.e. t_{35} to t_{38}. Figure 6.6 shows the improved detection performance for the new algorithm. There are two weak echoes in t_{35} and one weak echo in t_{37} detected by the new algorithm that are not detected by the conventional method.

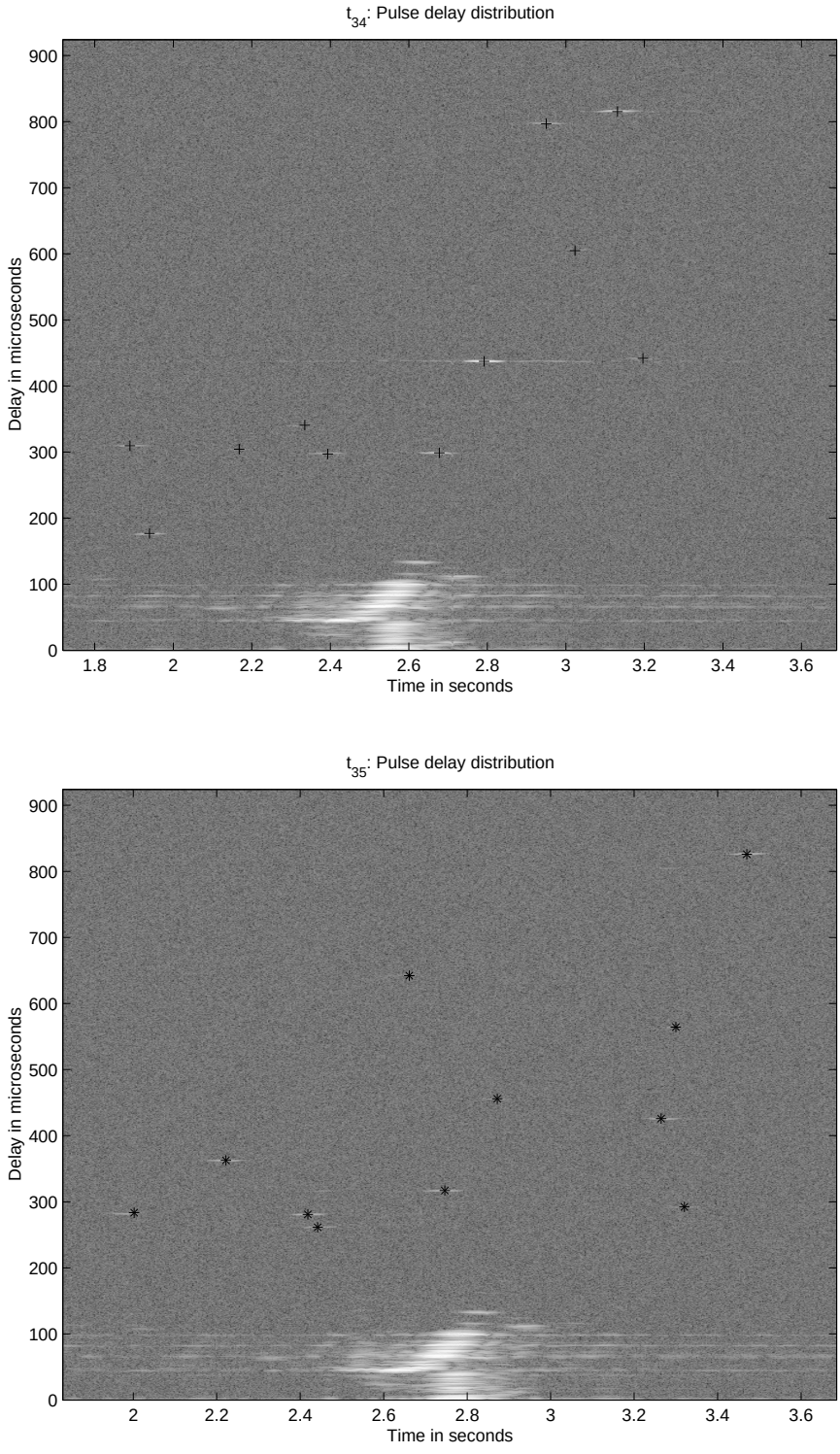

Figure 6.2: The pulse delay distribution and the detected echoes for data file t_{34} and t_{35}, where '+' and '*' mark detected pulses using the conventional tracker-detection.

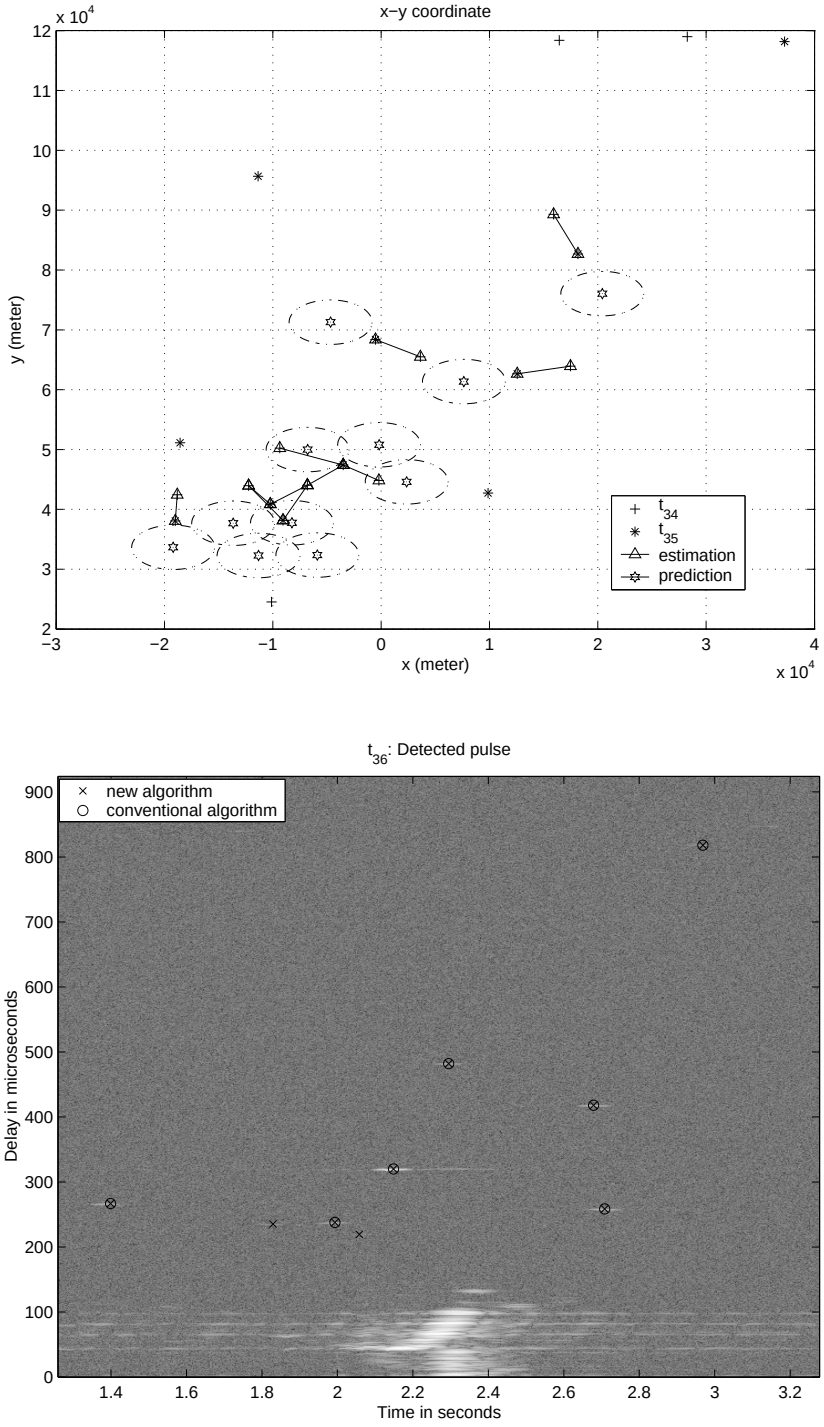

Figure 6.3: Tracking-detection process for data files: t_{36}. Figure in the top shows the prediction from Kalman tracker in x-y coordinate by using time-history information and the elliptical region around this prediction where we will utilize the decreased threshold. Figure in the bottom shows the detections by using conventional and old algorithms, respectively.

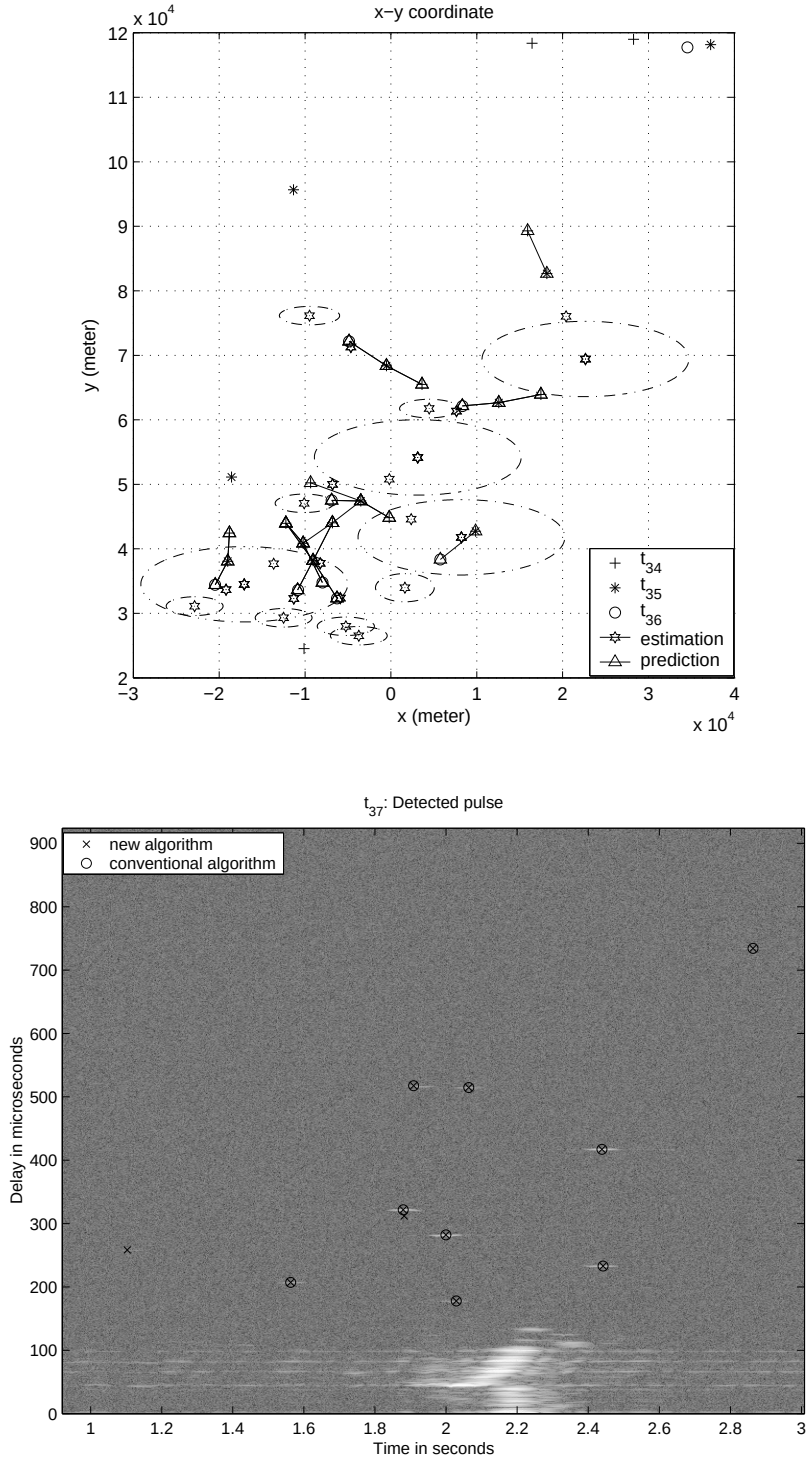

Figure 6.4: Tracking-detection process for data files: t_{37}. Figure in the top shows the prediction from Kalman tracker in x-y coordinate by using time-history information and the elliptical region around this prediction where we will utilize the decreased threshold. Figure in the bottom shows the detections by using conventional and old algorithms, respectively.

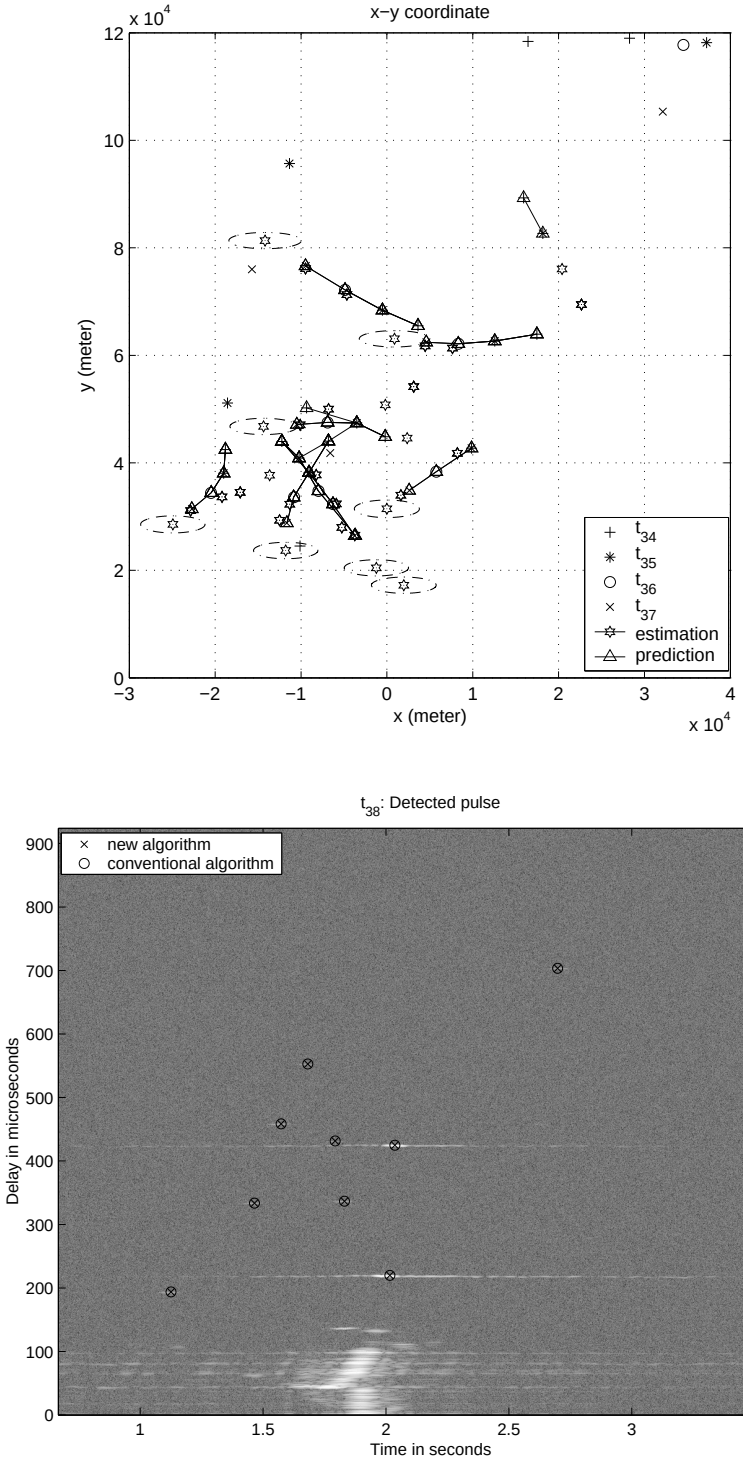

Figure 6.5: Tracking-detection process for data files: t_{38}. Figure in the top shows the prediction from Kalman tracker in x-y coordinate by using time-history information and the elliptical region around this prediction where we will utilize the decreased threshold. Figure in the bottom shows the detections by using conventional and old algorithms, respectively.

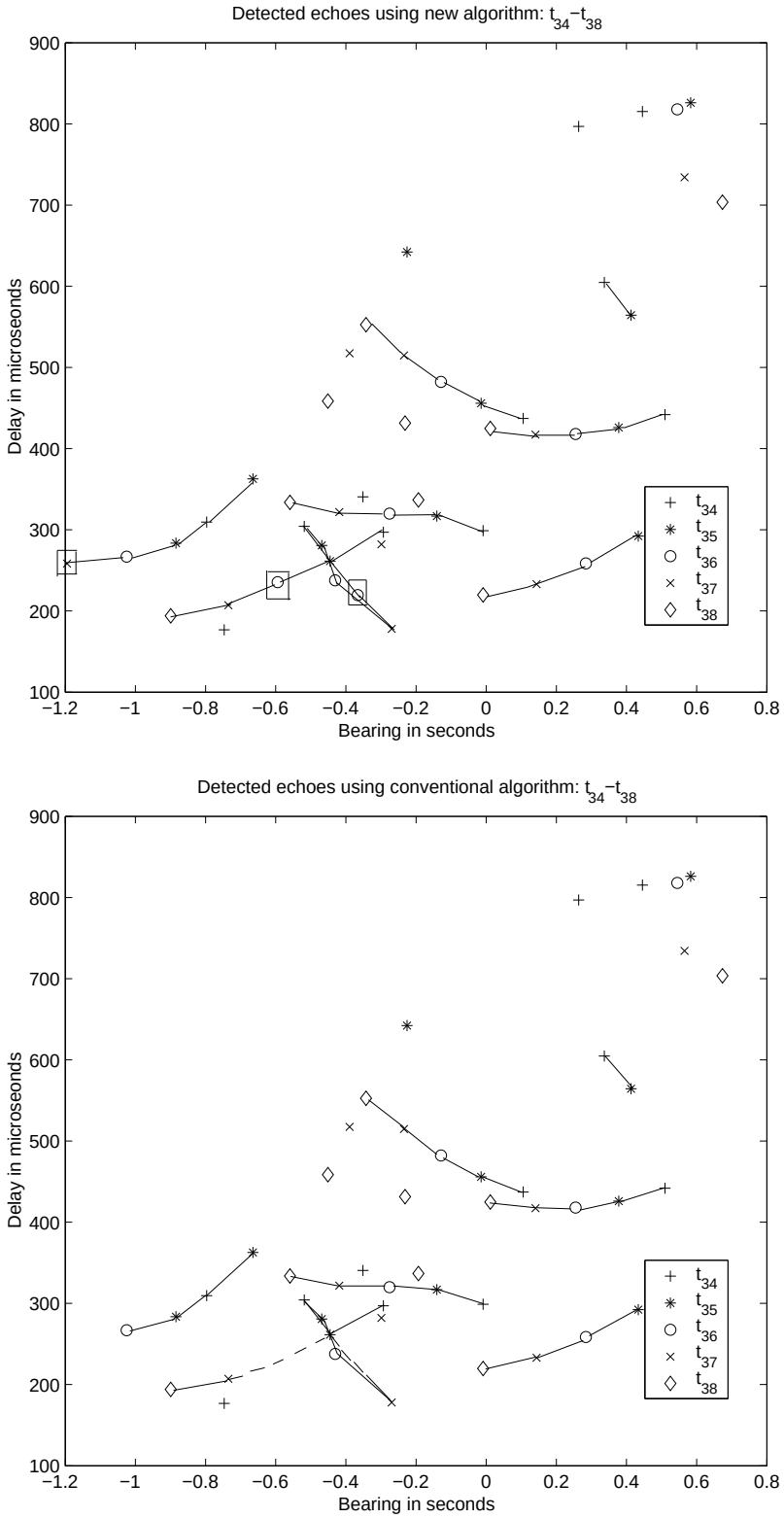

Figure 6.6: The detection results by using the new algorithm and the conventional one, respectively. Note that 3 weaker pulses (inside the rectangles) are detected by new algorithm.

6.2.2 Data Set 2

For data set 2, the echoes from local terrain and aircraft can be clearly seen when the RADAR beam is directly pointed to the GBT. So we will focus on only about two seconds of data in every other sweep when the RADAR beam passes directly over the GBT. We process the data only for every other sweep (such as the even data files t06, t08.....t34 here), because the data from continuous sweeps exhibit little movement between frames and the Kalman tracker works well with this "decimated" data. Figures 6.7 to 6.11 present the results for this data set. These figures are organized by time index order as follows: the two figures in every row show the tracking and detection process in two-second time interval in one sweep. The left one shows the prediction from the Kalman tracker in x-y coordinate by using time-history information, and the ellipse region around this prediction where we will utilize the decreased threshold. The right figure shows detections made using the conventional and old algorithms, respectively.

Figure 6.12 shows all the detections for the even numbered data files in data set two using the conventional and new algorithm, respectively. By using the tracker information, the new algorithm is able to detect some weaker echoes which are miss-detected by the conventional one, without increasing the false alarm detection significantly. As a comparison, we tried to detect those weaker echoes by decreasing the constant threshold for the conventional algorithm, as shown in the bottom plot of Figure 6.12. This scheme does pick up two weaker echoes (inside the squares), but also pick up four false alarm detections (inside the triangles) at the same time. So we conclude that the Bayesian combined tracking with detection algorithm did indeed improve the P_D v.s. P_{FA} performance in real data as expected.

6.3 Time Blanking Results

Our ultimate objective is to eliminate RADAR interference from the the data received at the telescope. To mitigate RADAR interference while preserving useful data, we propose a time blanking scheme based on the structure of the RADAR interference. The idea is to only perform the rejection in those time intervals during which

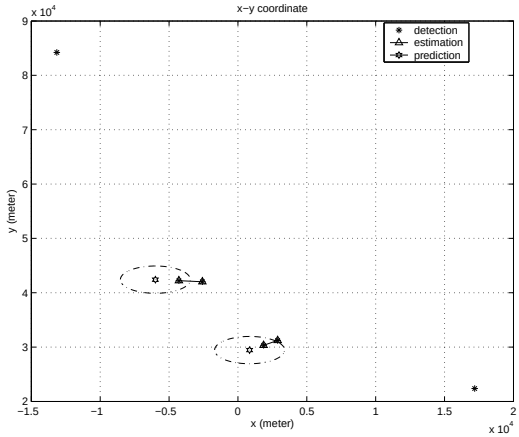

(t06:tracking)

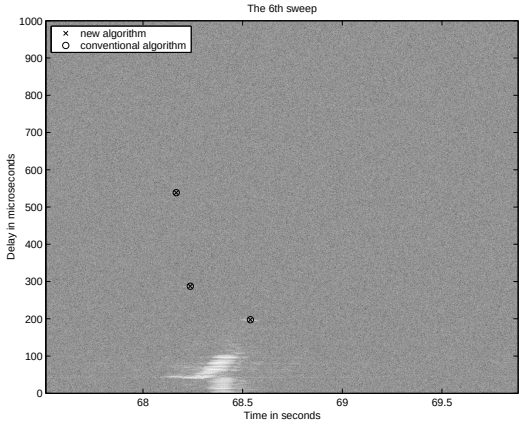

(t06:detecting)

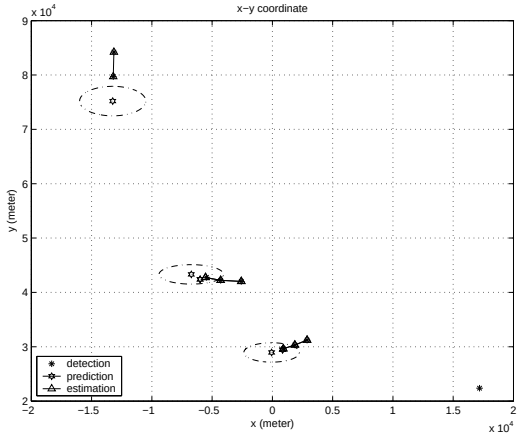

(t08:tracking)

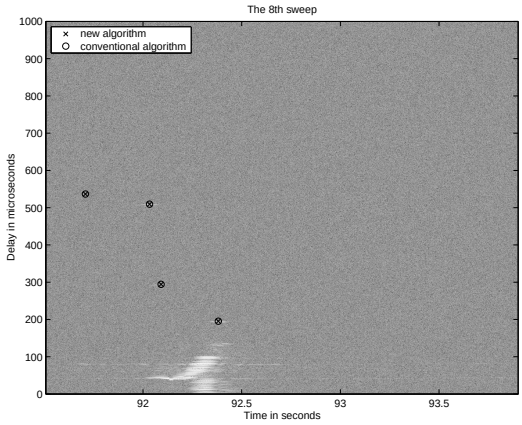

(t08:detecting)

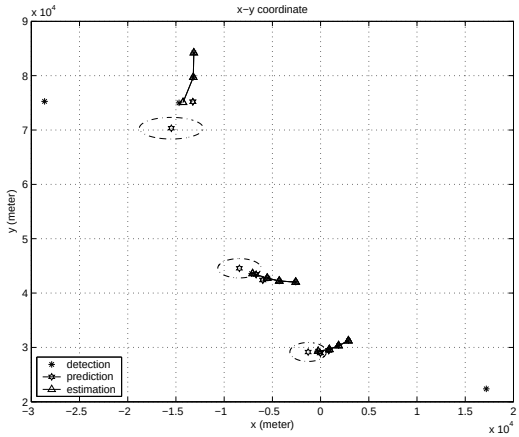

(t10:tracking)

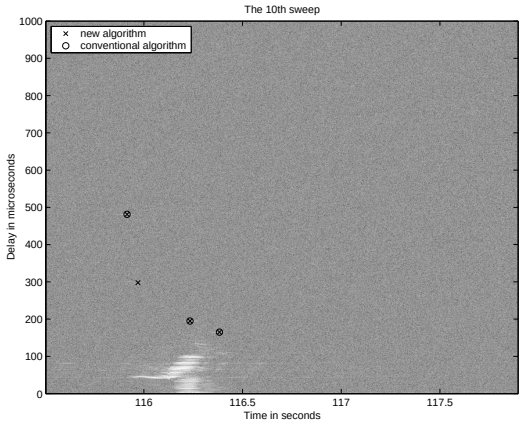

(t10:detecting)

Figure 6.7: Data files: t06, t08 and t10. In every data file process, first use Kalman tracking to locate the prediction, then use the new algorithm and the conventional one for detection, respectively.

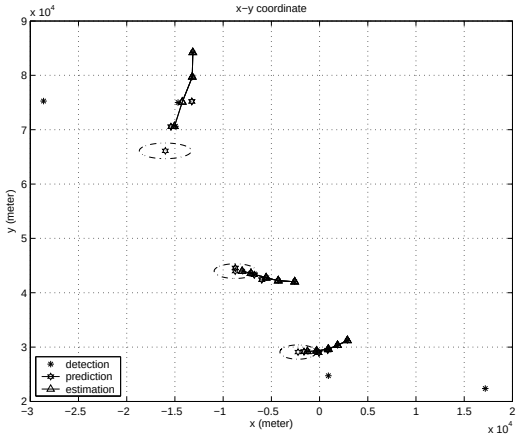

(t12:tracking)

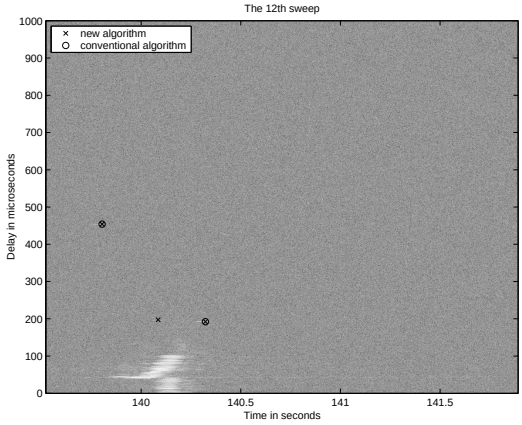

(t12:detecting)

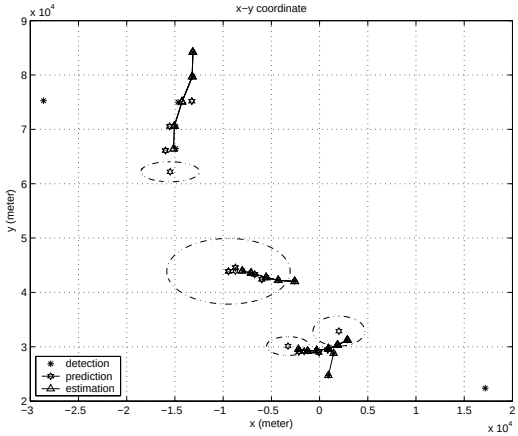

(t14:tracking)

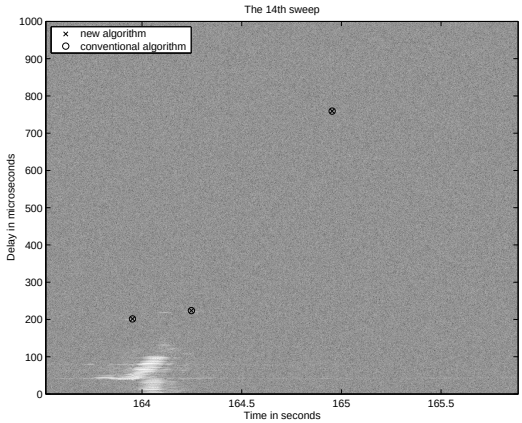

(t14:detecting)

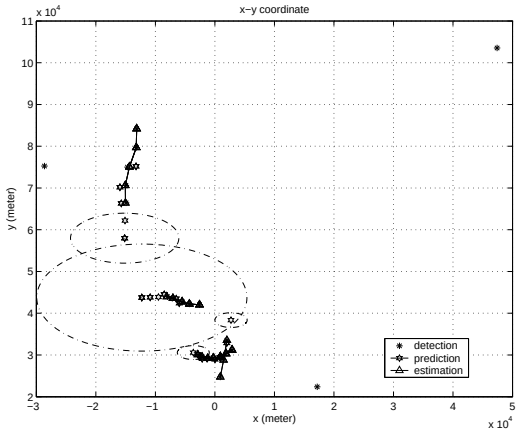

(t16:tracking)

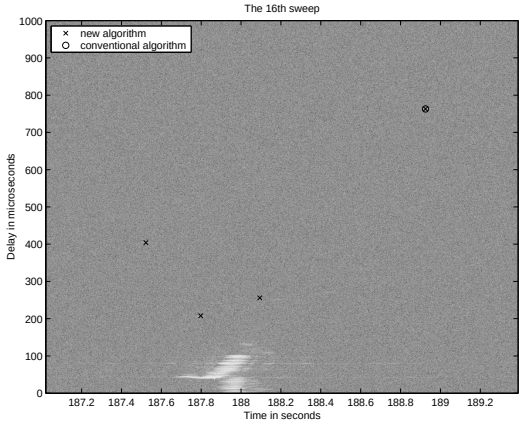

(t16:detecting)

Figure 6.8: Data files: t12, t14 and t16. In every data file process, first use Kalman tracking to locate the prediction, then use the new algorithm and the conventional one for detection, respectively.

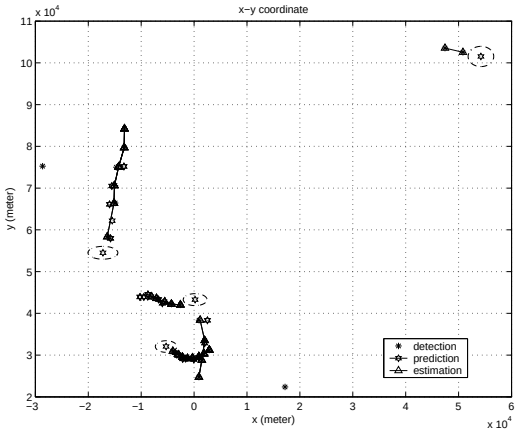

(t18:tracking)

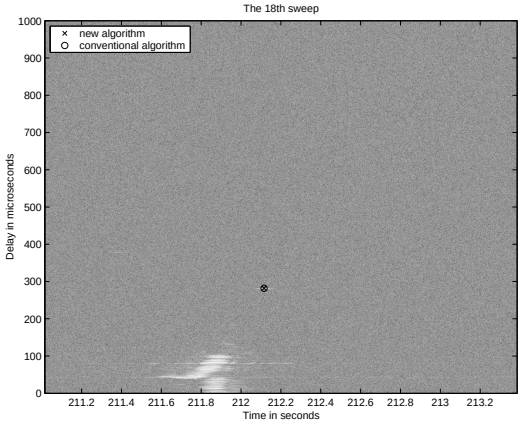

(t18:detecting)

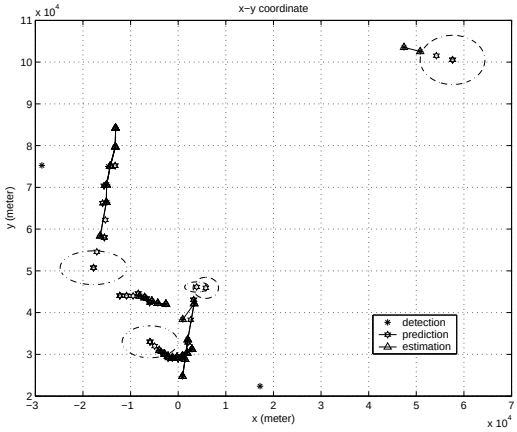

(t20:tracking)

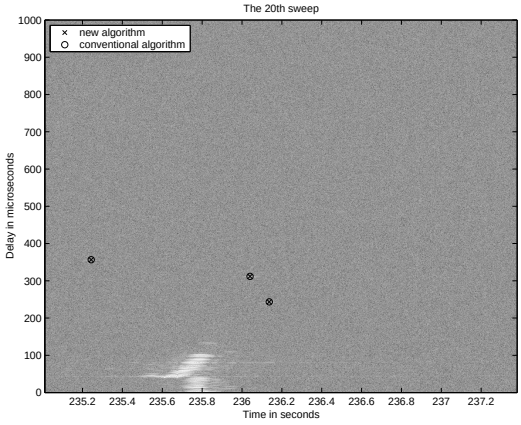

(t20:detecting)

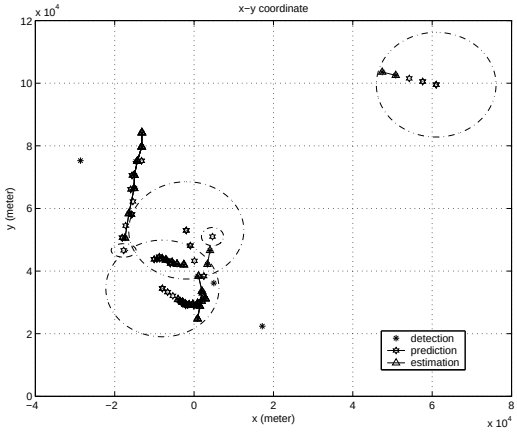

(t22:tracking)

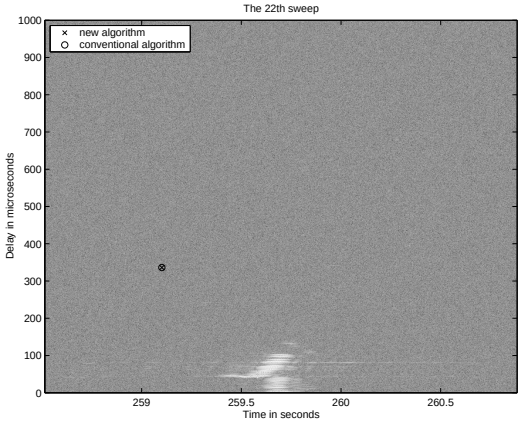

(t22:detecting)

Figure 6.9: Data files: t18, t20 and t22. In every data file process, first use Kalman tracking to locate the prediction, then use the new algorithm and the conventional one for detection, respectively.

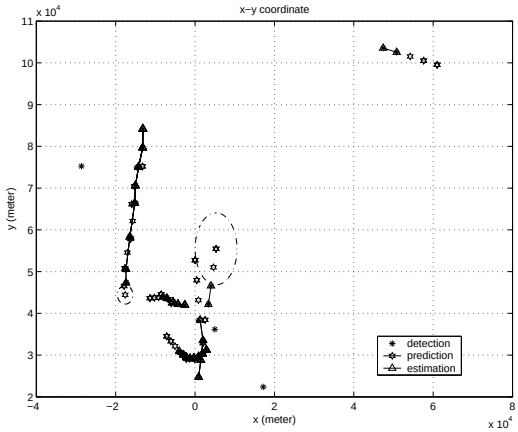

(t24:tracking)

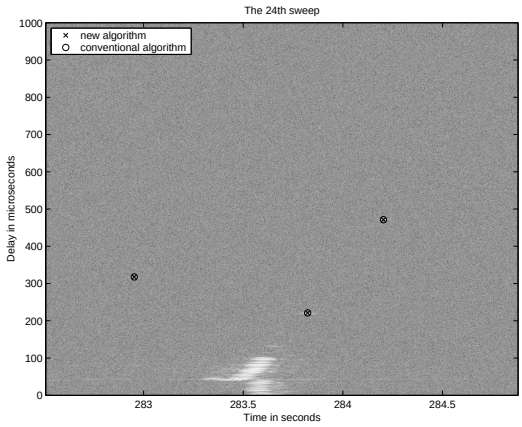

(t24:detecting)

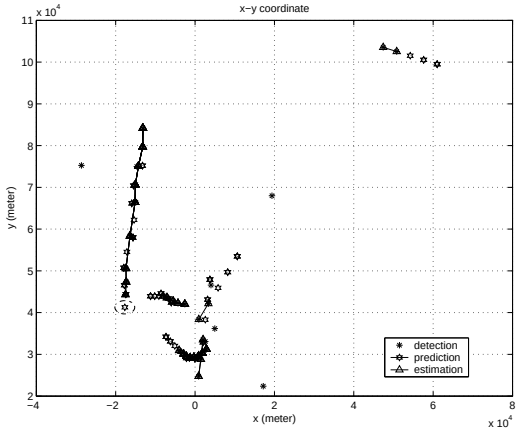

(t26:tracking)

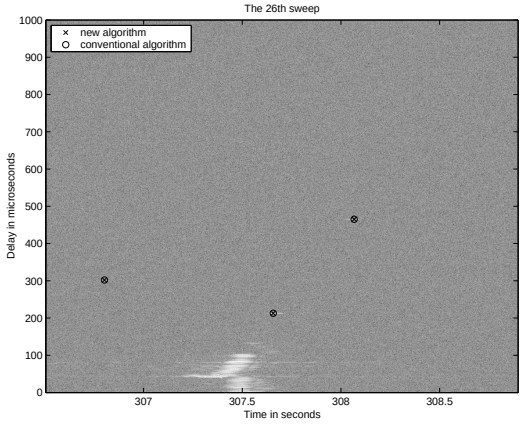

(t26:detecting)

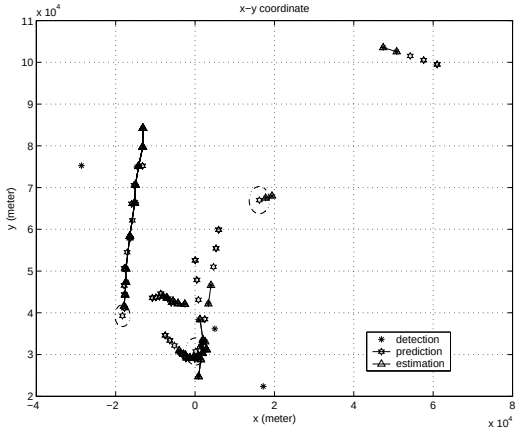

(t28:tracking)

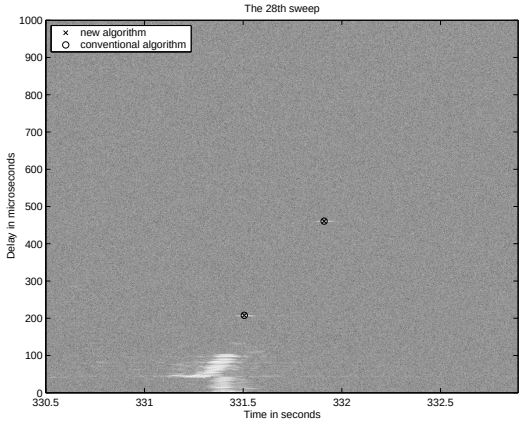

(t28:detecting)

Figure 6.10: Data files: t24, t26 and t28. In every data file process, first use Kalman tracking to locate the prediction, then use the new algorithm and the conventional one for detection, respectively.

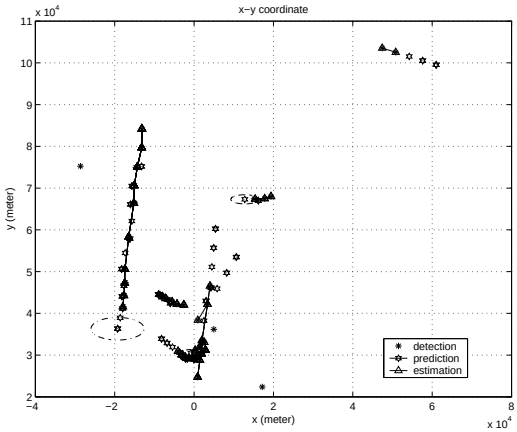

(t30:tracking)

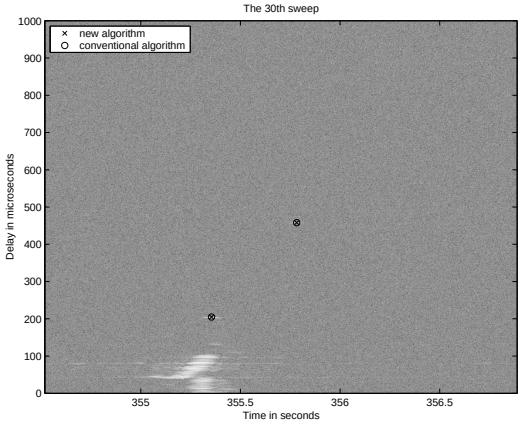

(t30:detecting)

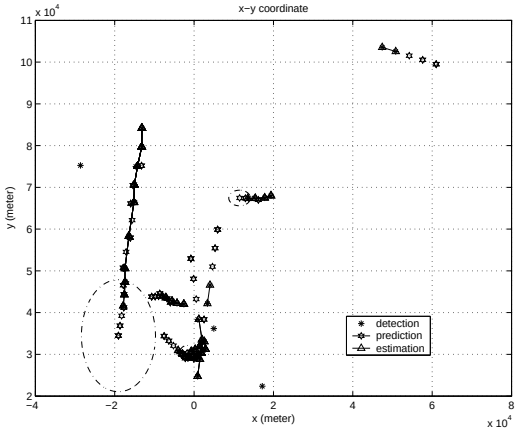

(t32:tracking)

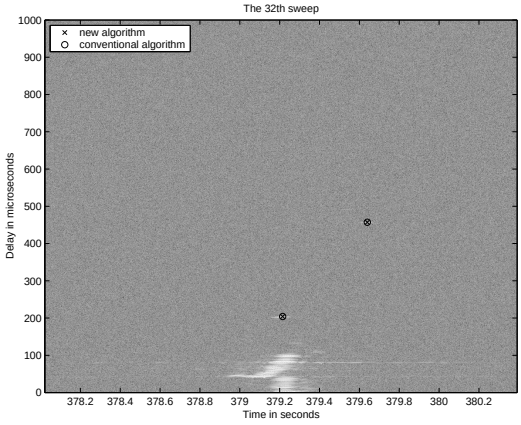

(t32:detecting)

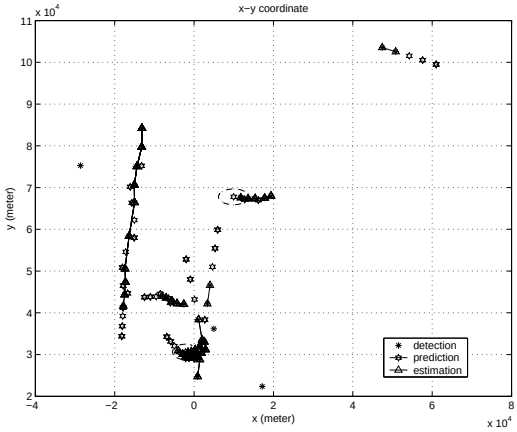

(t34:tracking)

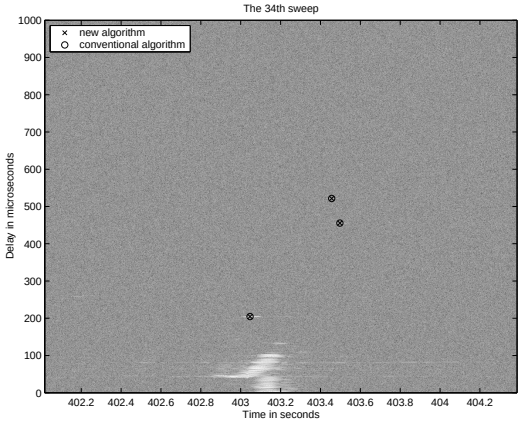

(t34:detecting)

Figure 6.11: Data files: t30, t32 and t34. In every data file process, first use Kalman tracking to locate the prediction, then use the new algorithm and the conventional one for detection, respectively.

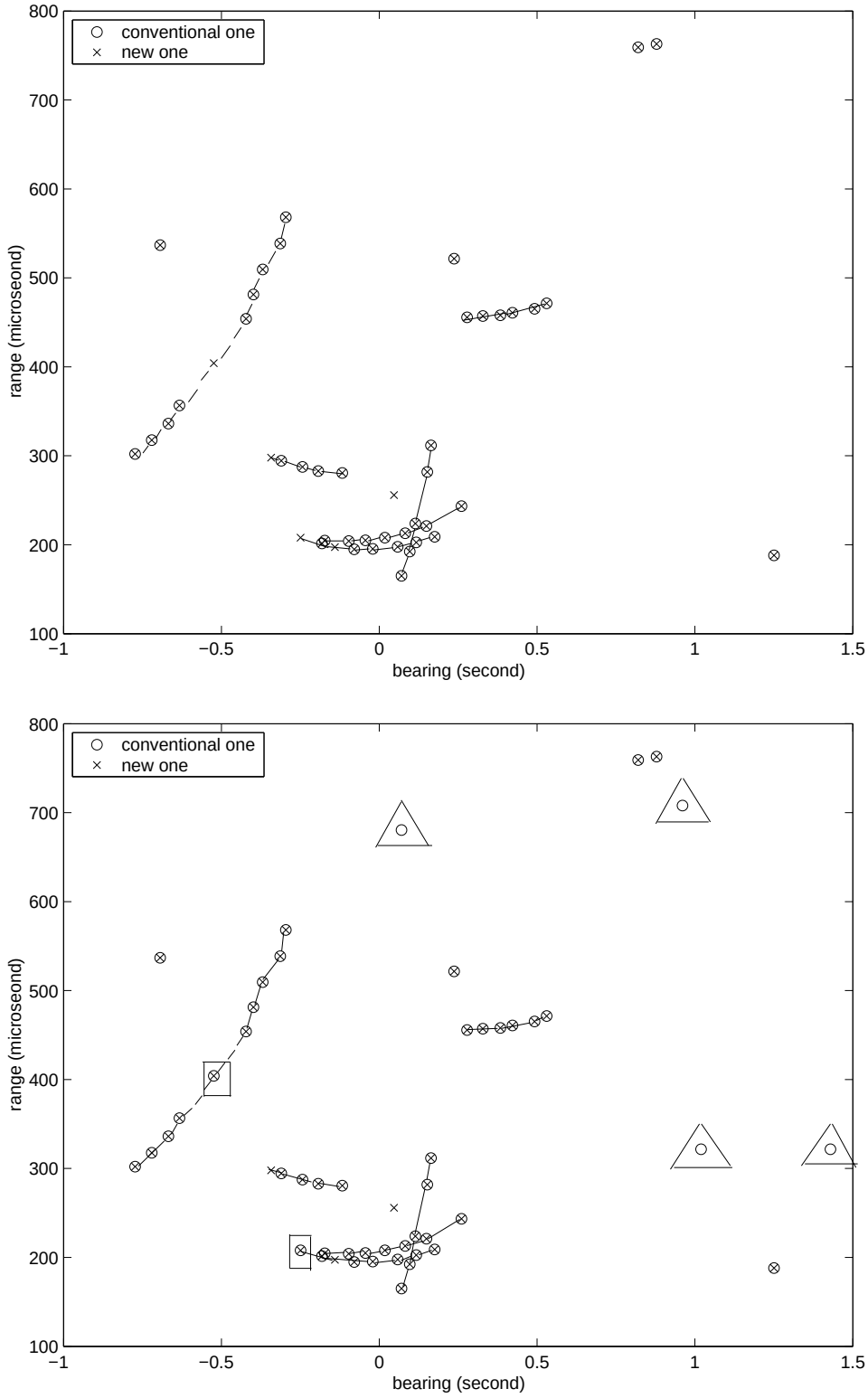

Figure 6.12: All the detections for the even data files in data set 2, using the new and conventional algorithms, respectively. The conventional detection algorithm sets the threshold by using $P_{FA} = 3.8676 * 10^{-8}$ for the top plot and $P_{FA} = 2.3205 * 10^{-7}$ for the bottom one.

the RADAR pulses are known to appear. Here we implement our blanker by "zero-stuffing", that is, putting zeros into the time samples where RADAR interference is detected.

6.3.1 Data Set 1

Three different techniques are tried on data set one in the time interval from 1.7 to 2.4 seconds (shown in figure 6.13) to determine whether the RADAR signal can be effectively removed from the spectrum:

- Simple time window blanking,
- Simple time window blanking with detected pulse blanking (using conventional pulse detection),
- Simple time window blanking with detected pulse blanking (using Bayesian combined tracking with detection algorithm).

There have been serval previous studies on this kind of blanking performance comparison [5][10][3].

In this work, the PSD is estimated by employing a 512-sample FFT with 50 percent overlap and a Hamming window. We use a reference spectrum to normalize the computed PSD so that we have a good measure of the effectiveness of the cancellation. This reference spectrum is obtained from the full 5 second data set in which the obvious pulses and all data 30 microseconds before, and 550 microseconds after, the predicted first arrival pulse are rejected. This rejection window guarantees that the reference signal is free of interference. The resulting reference spectrum is shown in Figure 6.14.

The normalized PSD, $\Phi(f)$, is given by [5][3]

$$\Phi(f) = \frac{S(f) - \hat{S}(f)}{\hat{S}(f)} \tag{6.3}$$

where f denotes the frequency, $S(f)$ represents the estimated PSD, and $\hat{S}(f)$ denotes the reference spectrum.

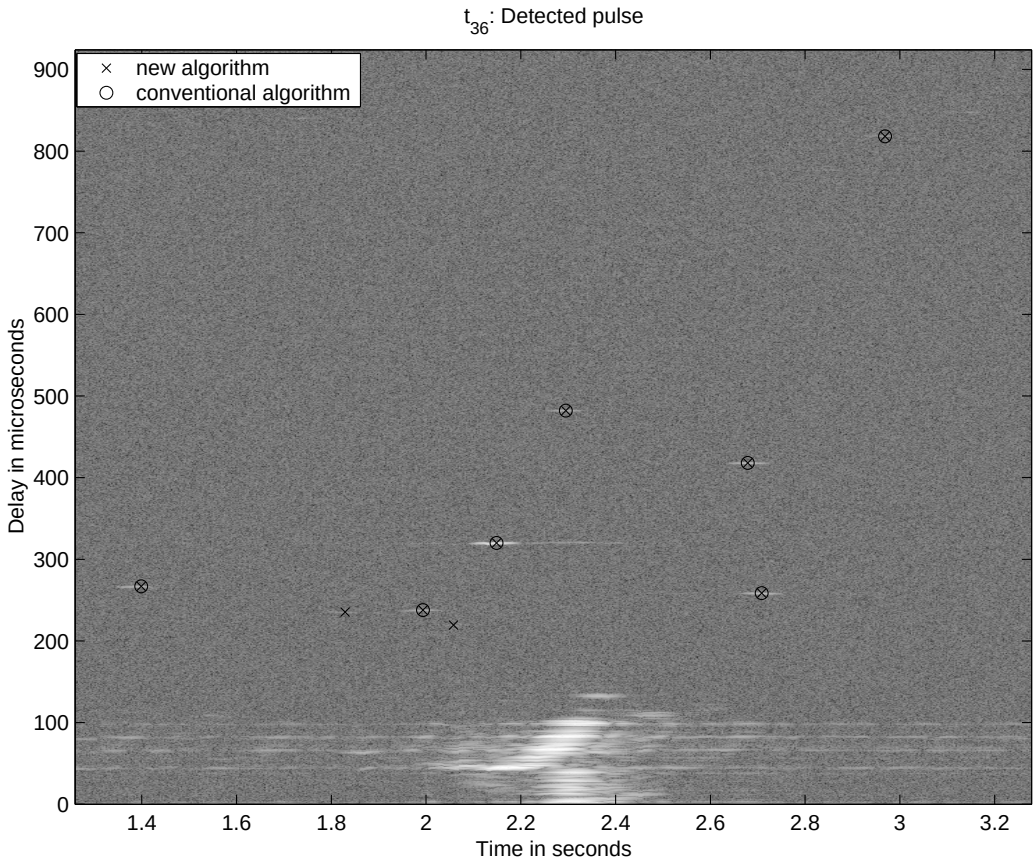

Figure 6.13: The data from 1.7 to 2.4 second is used to test and compare the blanking performance for three different techniques.

Figure 6.15 shows the unblanked spectrum accumulated over the 0.7-second interval when the radar beam was closest to the Green Bank azimuth. The top spectrum in Figure 6.16 shows the time window blanked spectrum accumulated over this same time interval but with time window blanking beginning 30 microseconds before and ending 150 microseconds after the first arriving pulses to encompass multipath echoes. This approach represents "simple time window blanking", and is similar to current practice at radio astronomy observatories. The samples within the window are rejected, while the samples outside the window remain intact. Thus, about 94 percent of the record is automatically preserved. As Figure 6.16 shows, the simple time window blanking does not completely eliminate the RADAR pulse from the

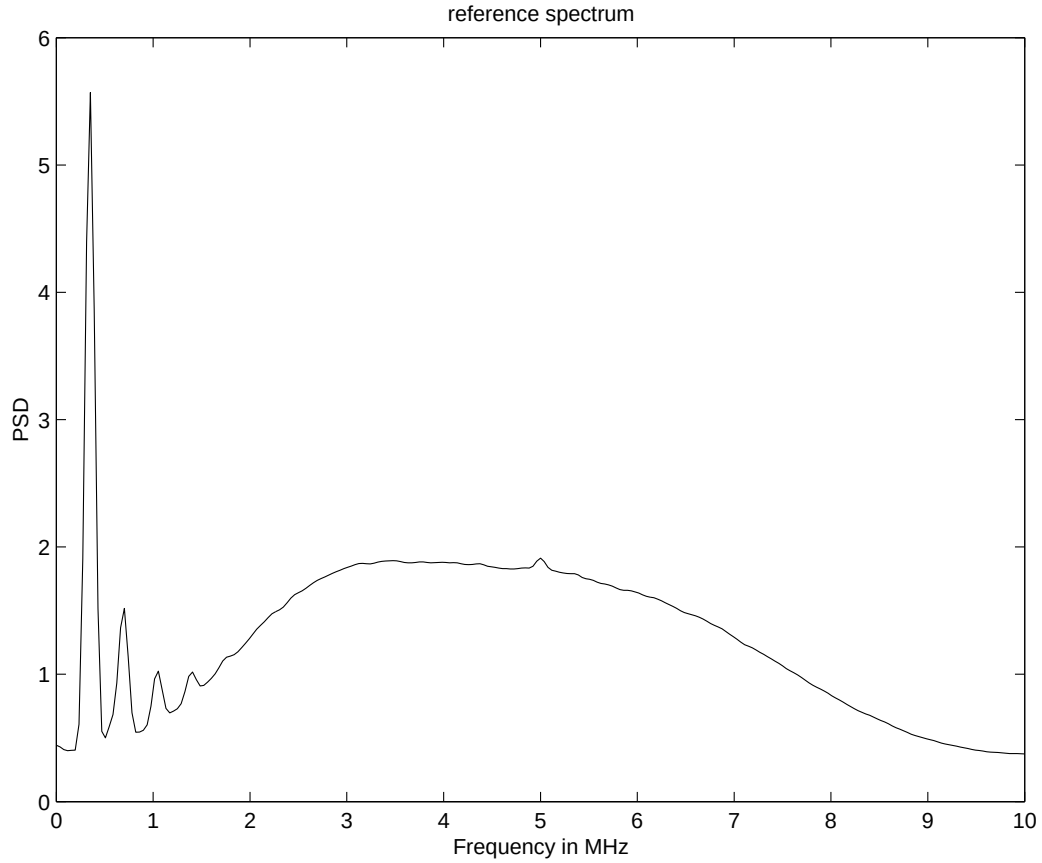

Figure 6.14: Initial reference spectrum.

spectrum. The reason for this defect is that the window fails to blank aircraft echoes. One obvious solution is to increase the window size to blank more pulses from the integration. But this will waste a lot of valuable data and the associated integration time.

We can improve blanking performance by combining pulse detected blanking with simple time window blanking. Pulse detected blanking is implemented by throwing away spectra that contain a detected pulse from the aircraft. Figure 6.16 compares the spectra from all the blanking methods. In order to make qualitative comparison, each estimate was normalized so that most of the spectral curves are aligned on top of each other. We can see that pulse detected blanking combined with time window blanking does eliminate the RADAR pulse completely from the spectrum. However

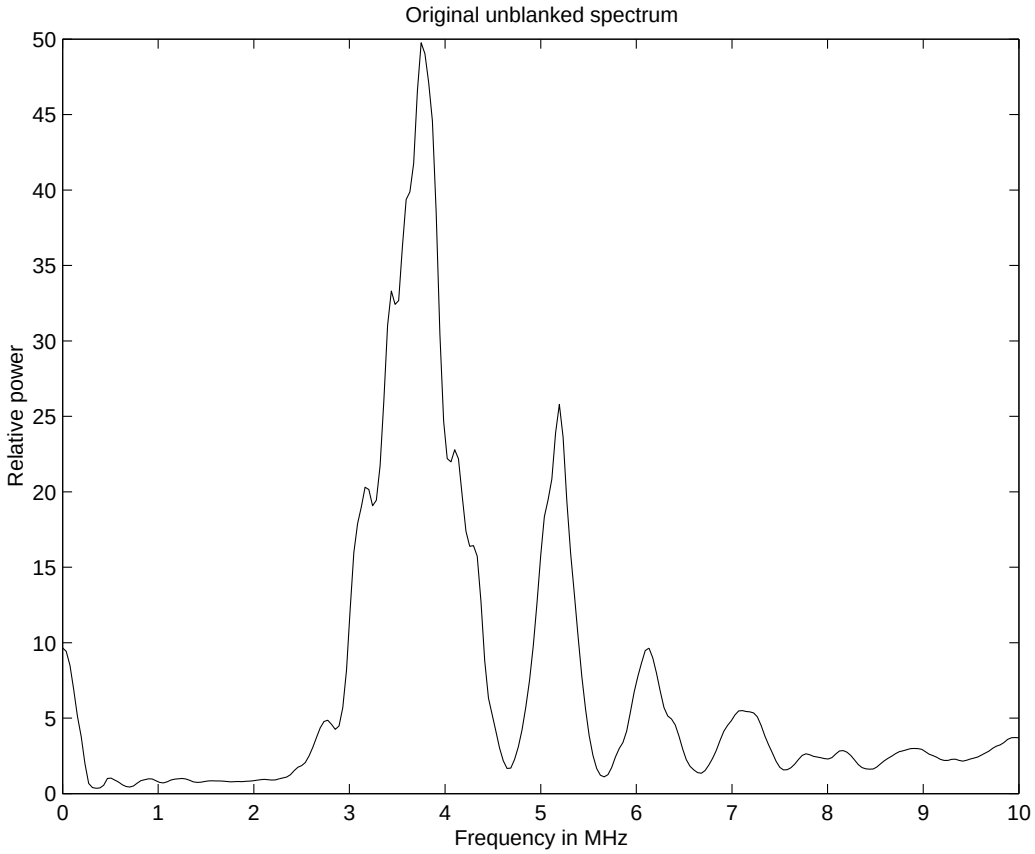

Figure 6.15: The unblanked spectrum integrated over to time when the RADAR beam was sweep over the GBT, between 1.7 and 2.4 seconds into the data shown as figure 6.13.

the difference between the pulse detection methods is not obvious. About 13.2 percent and 13.8 percent of the total data samples are rejected respectively in the integration for these two different pulse detected blanking algorithms.

6.3.2 Data Set 2

Three different blanking techniques are also tried on data set two in the time interval from 187.2 to 188.4 seconds (shown in figure 6.17).

Figure 6.18 shows unblanked spectrum in the time interval from 187.2 to 188.4 seconds and simple time window blanked spectrum accumulated over the same time interval but with time window blanking beginning 30 microseconds before and ending

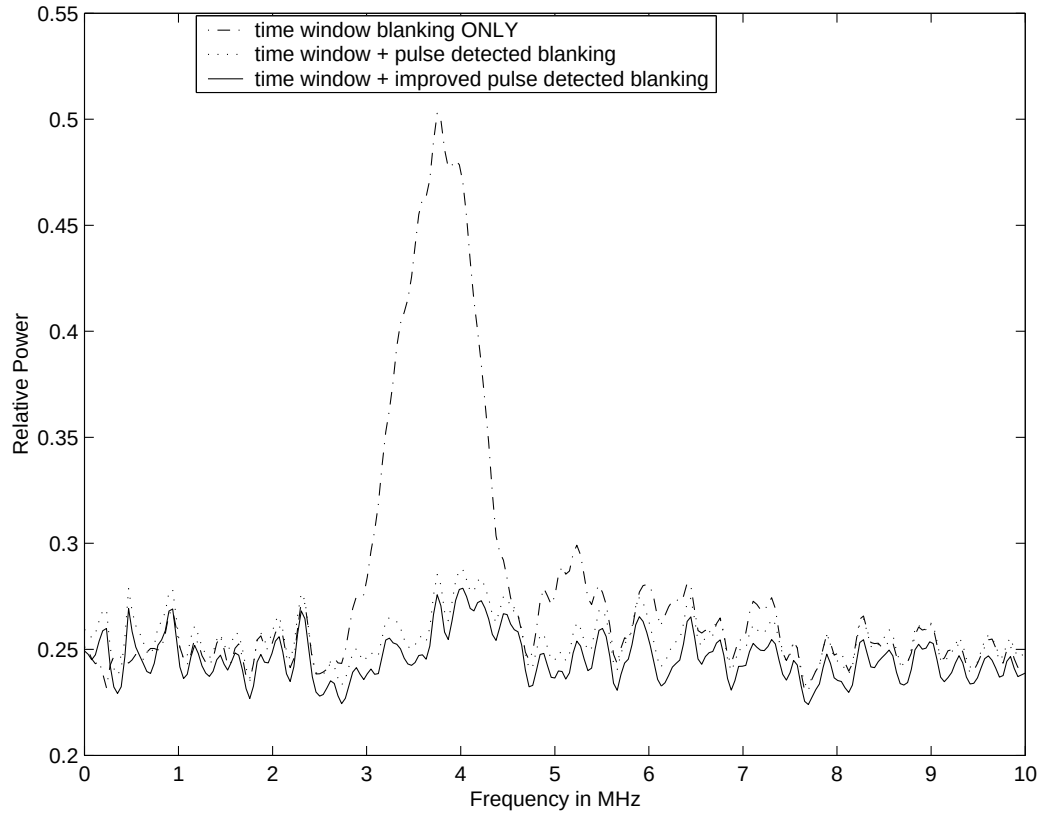

Figure 6.16: The spectra integrated in the same time interval with figure 6.15 from all the blanking methods: Top spectrum is for simple time window, which blanked 30 microseconds before and 150 microseconds after the earliest arriving pulses. Two bottom spectra are for window blanking combined with detected pulse blanking (conventional and new algorithms, respectively).

200 microseconds after the first arriving pulses spectra accumulated over the 1.2-second interval when the radar beam was closest to the Green Bank azimuth. About 93 percent of the record is automatically preserved for simple time window blanking.

As Figure 6.17 shows, during the time interval from 187.2 to 188.4 seconds, the new Bayesian combined tracking with detection algorithm detects three echoes, compared with no detection from the conventional pulse detection. So in this particular case, the spectrum for simple time window blanking with detected pulse blanking using conventional pulse detection will have the same blanking performance with simple time window blanking. Figure 6.19 compares the spectra from all the blanking

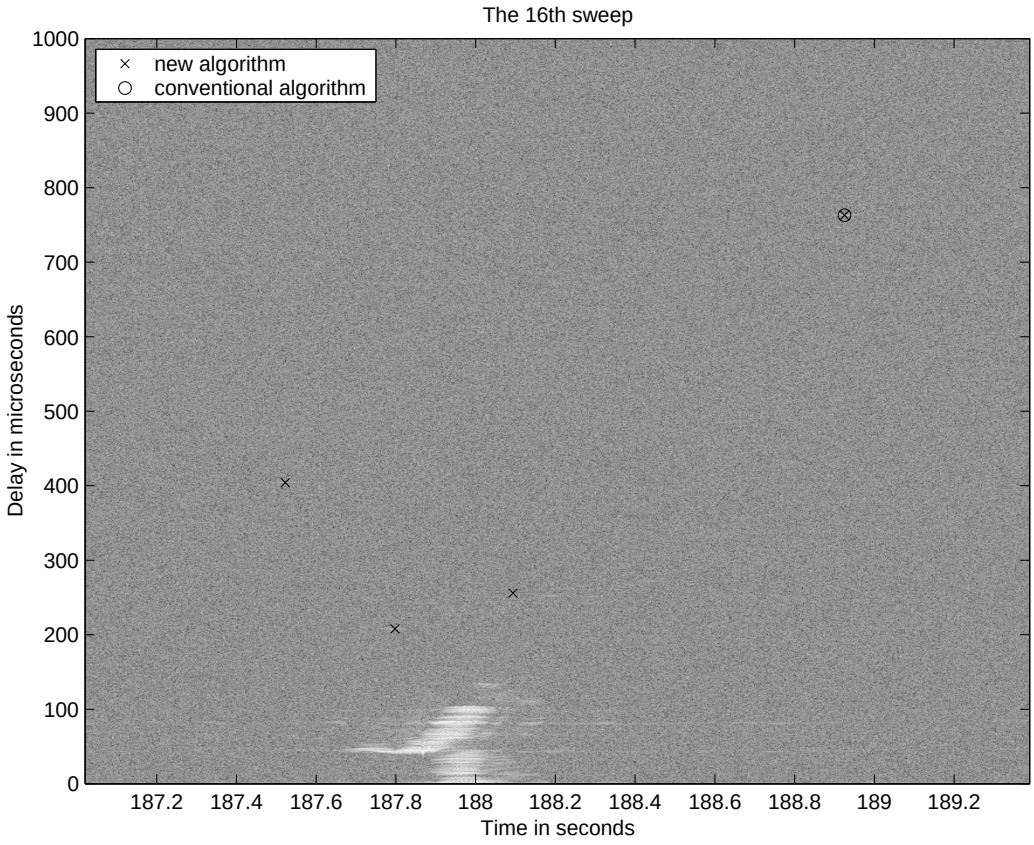

Figure 6.17: The data from 187.2 to 188.4 seconds is used to test and compare the blanking performance for three different techniques.

methods. In order to make qualitative comparison, each estimate was normalized so that most of the spectral curves are aligned on top of each other. We note that pulse detected blanking combined with simple time window blanking does eliminate the RADAR pulse completely from the spectrum. Here we are also able to tell the difference between the pulse detection methods.

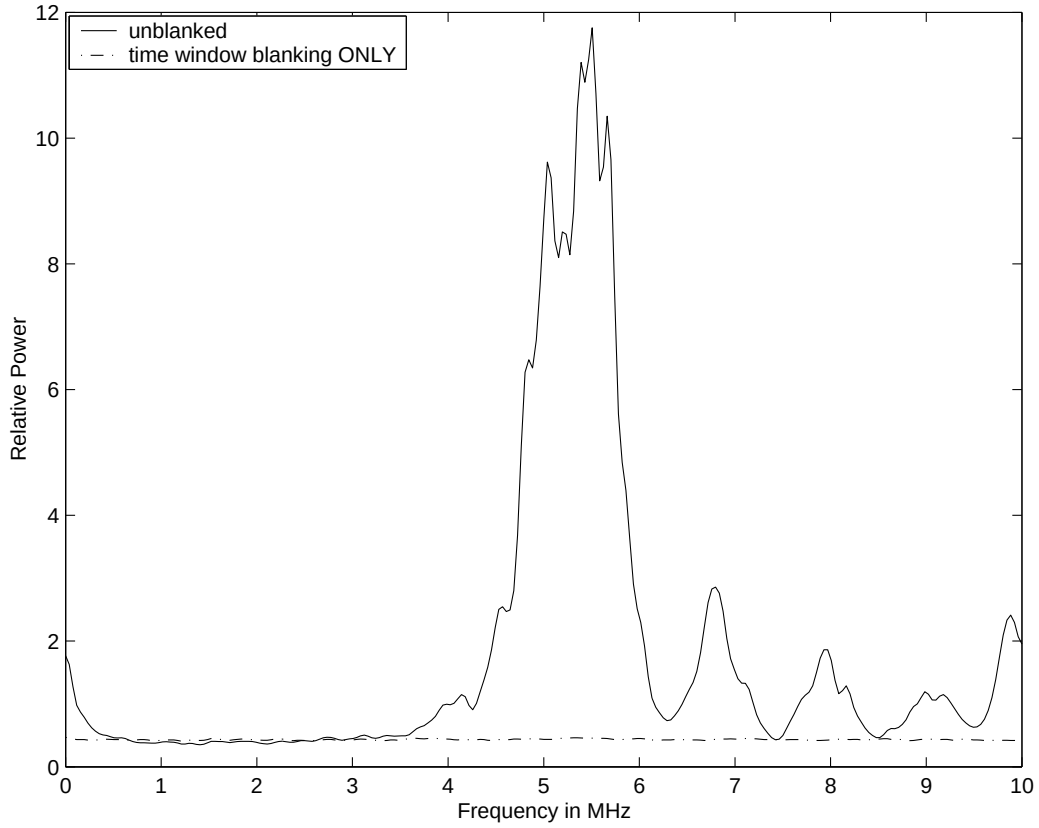

Figure 6.18: The unblanked and simple time window blanked spectra integrated over to time when the RADAR beam was sweep over the GBT, between 187.2 and 188.4 seconds into the data shown as figure 6.17.

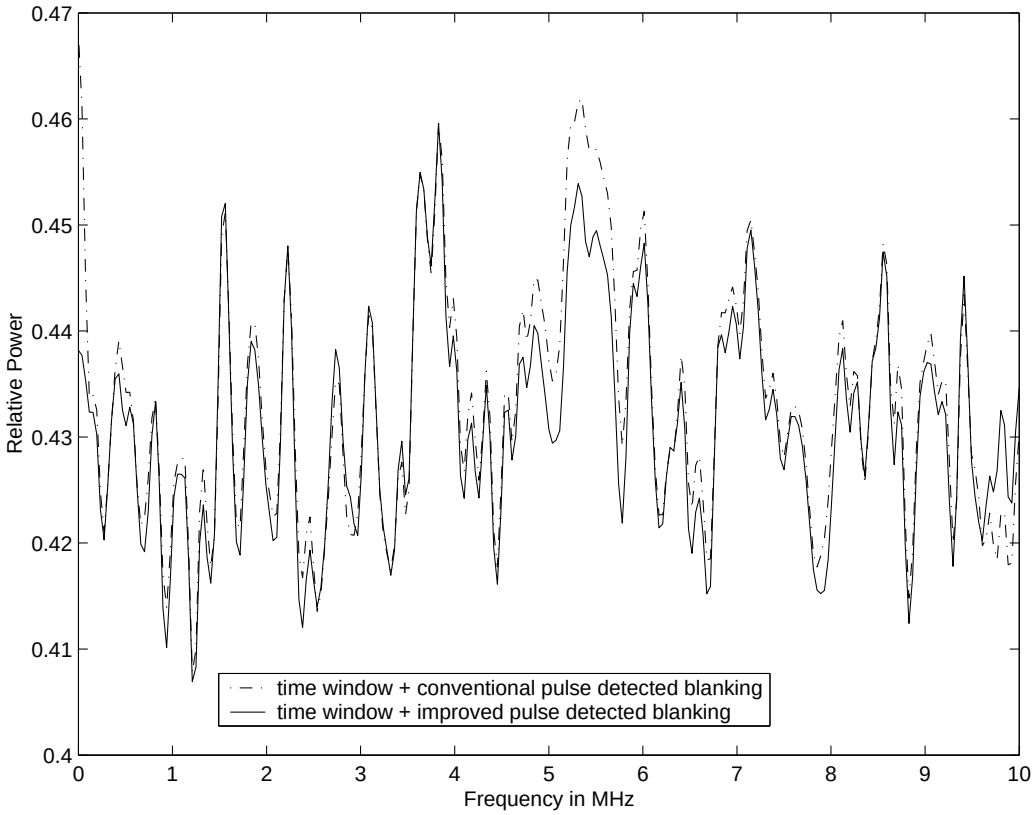

Figure 6.19: The spectra with simple time window blanking combined with detected pulse blanking (using new and conventional echo detection algorithms, respectively)
.

Chapter 7

Conclusions

In this thesis, we have combined two blanking approaches, time window blanking and detected pulse blanking, to mitigate RADAR RFI at the GBT. To achieve better performance for detected pulse blanking, we proposed a new Bayesian combined tracking with detection algorithm. This helps to locate the weaker aircraft echoes, so as to help improve performance of detected pulse blanking. The experiments in Chapter 6 prove that combining this Bayesian detection pulse blanking with time window blanking achieves the advantages of both approaches, that is, it eliminates as much as interference as possible, such as the strong pulses from terrain reflection, but also removes only the corrupted data, such as those isolated aircraft echoes, without sacrificing neighboring data unnecessarily.

Scientists at the GBT have tried different blanking techniques to separate RADAR RFI from cosmic signal. The most popular way is to use time window blanking to remove all data that could possibly contain echoes on direct path signals. However, this is not completely effective, because of the loss of integration time. A large fraction of the time between RADAR pulses cannot be used for high sensitivity spectral line measurements. An alternative is detected pulse blanking, which retains more useful integration time, but runs the risk of failing to blank some weaker echoes. So detected pulse blanking is not a usable technique on its own, but it can be used to reject long-delay pulse reflection that falls outside of the selected blanking time window. The new Bayesian combined tracking with detection algorithm provides a very important method to combine these two techniques and significantly improve pulse detection performance.

There are some new and unique contributions about this work:

- First to use Kalman tracking to enable real time blanking for RADAR pulse detection RFI mitigation in radio astronomy.
- First to use a Kalman tracker in a Bayesian detection framework for RADAR echoes to improve detection sensitivity. This is particularly important in radio astronomy where even echoes below the noise floor can bias cosmic signal spectral.
- Demonstrated operation with two real data sets from the GBT.
- Demonstrated the ability to create and maintain multiple simultaneous tracks.

To put this work into practice for the astronomers in the GBT, there are few issues which need to be solved:

- To realize real-time pulse detection, we will have to use a high speed DSP processor and adapt the algorithm code for to a high speed DSP platform. The RADAR receiver described in Section 3.1- 3.3 could be implemented in the same DSP that Andrew Poulsen used for real-time GLONASS adaptive cancellation [22].
- Kalman tracking and blanking has sufficiently low computational demands that it can be implemented in a modest host personal computer in real time, but this would require new code development.
- Because of limited memory, we must buffer the data on a hard drive prior to analysis using Matlab codes for post processing.

Further extension to this work will consider a more complicated blanking technique than simply stuffing zero in the pulse structure when a pulse is detected.

Bibliography

[1] G. C. Bower, "Radio Frequency Interference Mitigation", Tech. Rep., UC Berkeley Radio Astronomy Laboratory, 2003.

[2] P. A. Fridman and W. A. Baan, "RFI Mitigation Methods in Radio Astronomy", *Astronomy and Astrophysics*, vol. 378, pp. 327–344, 2001.

[3] Q. Zhang, Y. Zheng, S. G. Wilson, J. R. Fisher, and R. Bradley, "Combating Pulsed Radar Interference in Radio Astronomy", *The Astronomical Journal*, vol. 126, 2003.

[4] Ph. Ravier and R. Weber, "Robustness in the RFI Detection for Time-Blanking", Tech. Rep., LESI and ESPEO, University of Orlans, France, 2000.

[5] J. R. Fisher, "Analysis of Radar Data from February 6, 2001", Tech. Rep., National Radio Astronomy Observatory, 2001.

[6] J. R. Fisher, "RFI Propagation Paths", Tech. Rep., National Radio Astronomy Observatory, 2003.

[7] A. Leshem and A-J. van der Veen, "Introduction to Interference Mitigation Techniques in Radio Astronomy", *Perspectives in Radio Astronomy: Technologies for Large Antenna Arrays*, 1999.

[8] A. Leshem and A-J. van der Veen, "Blanking of TDMA signals and its Effect on Radio-Astronomical Correlations Measurements.", *Proc. HOS99*, 1999.

[9] S. W. Ellingson and G. A. Hampson, "RFI and Asynchronous Pulse Blanking in the 12301375 MHz Band at Arecibo", Tech. Rep., Ohio State University, 2002.

[10] S. W. Ellingson and G. A. Hampson, "Mitigation of Radar Interfernece in L-Band Radio Astronomy", *Astrophysical Journal Supplement Series*, vol. 147, pp. 167–176, 2003.

[11] H́ogbom, "Aperture Synthesis with a Non-Regular Distribution of Interferometer Baselines", *Astr. Astrophys. Suppl.,*, vol. 15, pp. 417, 1974.

[12] D. J. Sakrison, *Communication theory: Transmission of Waveforms and Digital Information*, Wiley and Sons, Incorporated, John, 1968.

[13] J. Kirkhorn, "Introduction to IQ-demodulation of RF-data", Tech. Rep., IFBT, NTUN, 1999.

[14] N. E. Bylund, M. Andersson, and H. Knutsson, "Wide range frequency estimation in ultrasound images", in *Proceedings of the SSAB Symposium on Image Analysis*, Linköping University, Sweden, 2001.

[15] A. R. Thompson, J. M. Moran, and Jr. G. W. Swenson, *Interferometry and Synthesis in Radio Astronomy*, Wiley, New York, 1986.

[16] S. Horiuchi, S. Kameno, and M. Ohishi, "Developing a Wavelet CLEAN Algorithm for Radio-Interferometer Imaging", *Astronomical Data Analysis Software and Systems X, ASP Conference Series,*, vol. 238, 2001.

[17] B. D. Jeffs, E. Pyper, and B. Hunter, "A wireless MIMO Channel Probing Approach for Abritrary Antenna Arrays", Tech. Rep., Brigham Young University, 2001.

[18] T. K. Moon and W. C. Stirling, *Mathematical Methods and Algorithms for Signal Processing*, Prentice Hall, 2000.

[19] K. V. Ramachandra, *Kalman Filtering Techniques for Radar Tracking*, Marcel Dekker, Inc, 2000.

[20] P. Zarchan and H. Musoff, "Fundamentals of Kalman Filtering: A Practical Approach", *Progress in Astronautics and Aeronautics*, vol. 190, pp. 257–291, 2000.

[21] B. R. Mahafza, *Radar Systems Analysis and Design Using MATLAB*, Chapman and Hall/CRC, 2000.

[22] A. J. Poulsen, *Real-Time Adaptive Cancellation of Satellite Interference in Radio Astronomy*, Master's thesis, Brigham Young University, 2003.

[23] T. E. Gergely A. R. Thompson and P. A. Vanden Bout, "Interference and Radioastronomy", *Physics Today*, vol. 44, pp. 41–49, 1991.

[24] T. A. Th. Spoelstra, "Reduction of Interference in Radio Astronomy", in *Proceedings of the 12th International Wroclaw Symposium on Electromagnetic Compatibility*, 1994.

[25] "Interference Identification and Excision", in *Proceedings of the Radio Astronomy Workshop*, NRAO, Green Bank, West Virginia, 1982.

[26] P. A. Fridman, "Radio Frequency Interference Rejection in Radio Astronomy Receivers", *Proc.Eusipco-98*, vol. 4, pp. 2241–2243, 1998.

[27] R. Ghose, *Interference Mitigation Theory and Application*, IEEE Press, Piscataway, NJ, 1996.

[28] J. R. Fisher, "The Nature of RFI and Some Lines of Defense", in *Proceedings of International Astronomical Union Colloquium No.112*, NRAO, Green Bank, West Virginia, 1991.

[29] S. W. Ellingson and G. A. Hampson, "A Subspace-Tracking Approach to Interference Nulling for Phased Array-Based Radio Telescopes", *IEEE Trans. Antennas and Propagation,*, vol. 50, pp. 25–30, 2002.